OpenFOAM® Journal

Volume 6 [Full Papers], Pages 25–50
ISSN: 2753-8168

Numerical Study on the Application of Overset Mesh Method for Rotating Impellers Using OpenFOAM®

Mari Niemelä[1,*], Ville Vuorinen[2], Mikko Kanerva[3], Riku Sundell[4], and Minna Kellomäki[1]

[1]Faculty of Medicine and Health Technology, Tampere University, Tampere 33720, Finland
Email address: mari.niemela@tuni.fi

[2]Department of Energy and Mechanical Engineering, Aalto University, Espoo 02150, Finland

[3]Faculty of Engineering and Natural Sciences, Tampere University, Tampere 33720, Finland

[4]Bayer Oy, Pharmaceutical Sciences, Turku 20101, Finland

DOI: https://doi.org/10.51560/ofj.v6.163
Results with version(s): OpenFOAM® v2306
Repository: -

Abstract. Intermeshing rotors exist in various applications, such as kneaders and extruders, and their performance could be assessed using computational fluid dynamics simulations. It is essential to evaluate the robustness and accuracy of such simulations. Here, we apply the overset mesh method to simulate intermeshing rotors using a Newtonian fluid to assess the suitability of the method. First, the simulations of concentric cylinders were used to evaluate the effect of three numerical approaches. Second, the simulations of a rotating impeller were applied to study five different mesh topologies. Finally, two intermeshing impellers were simulated to demonstrate the functionality of the overset mesh method, and the conservation of transported scalar was evaluated. All cases were simulated using the OpenFOAM open-source software. The general observations were: 1) The simulated velocity fields were in good accordance with the reference cases and the passive scalar was conserved in the simulation case of intermeshing impellers despite the inherent mass conservation errors. 2) However, fluctuations in power number were detected for conformal meshes in the two impeller case.

1. Introduction

Various applications utilize intermeshing rotors, i.e. rotors which come close to each other and have intersecting sweep areas. The geometry of the rotors can be different, for example, they can be impellers in kneaders or screws in twin screw extruders (TSEs). These applications are often designed and optimized using the experimental trial-and-error -approach which requires resources significantly. An alternative to the experimental approach is provided by numerical analysis utilizing computational fluid dynamics (CFD). The main challenges in simulating intermeshing rotors are related to the rotating geometries, the existing narrow gaps, and the intersecting sweep areas. The rotating geometries induce large relative motions between the rotors and the stationary walls. These motions distort the mesh used in CFD simulations, affecting the quality of the mesh and consequently, the accuracy of the simulation. In the narrow gaps, high mesh density is required for accurate simulation, and the large relative motions distort the mesh substantially. The intersecting sweep areas have overlapping domains which cannot be simulated using conventional mesh methods, such as sliding meshes.

Several numerical CFD methods have been used to simulate intermeshing rotors. In the finite element method (FEM), quasi steady state simulations of TSEs [1,2] have been studied using remeshing method for the rotating geometries. However, this method is very time-consuming. Therefore, other methods have been developed including the mesh superposition technique (MST) and the fictitious domain method (FDM). In the MST [3], independent meshes are constructed for the fluid and the rotors. The position of the rotors is updated at each time step, and it is detected whether the nodes of the fluid mesh are in the fluid region or the rotor region. In the fluid region, the velocity is calculated according to the

* Corresponding author

Received: 16 June 2025, Accepted: 2 January 2026, Published: 8 March 2026

governing equations, but in the rotor region, a penalty formulation is used to match the velocity to the screw velocity. This method has been applied e.g. to kneaders [4, 5] and TSEs [6–8]. The FDM [9] is analogous to MST, but Lagrange multipliers are utilized instead of the penalty technique, to include the rotating geometries. This method has been used e.g. for a helical ribbon mixer [10]. However, both MST and FDM have certain disadvantages. Alsteens [11] noted that mass conservation in these methods is not guaranteed. Giguère et al. [10] stated that mesh refinement is required for MTS to improve the mass conservation and to obtain a good description of the moving rotors, especially in the narrow gaps. Sarhangi Fard et al. [12] noted that FDM had fundamental accuracy issues mainly in the narrow gap regions despite the local mesh refinement.

In the finite volume method (FVM), the rotating geometry of intermeshing rotors has been simulated using the overset mesh (also referred to as Chimera mesh) method. In the overset mesh method [13], the stationary background mesh covers the computational domain completely and dynamic meshes are created around the moving rotors. These separate meshes overlap, and the information between the meshes is exchanged via interpolation on specified cells. This method has been applied, for example, to a mixer [14] and helicopter rotors [15]. The advantages [16] of the overset mesh method are its potential for simulating large relative motions, the simplified grid generation of the individual meshes, and the consequent improvement of the mesh quality. The challenges [16–18] of this method are related to mass conservation: the FVM utilizing overset mesh method becomes non-conservative due to the interpolation between the meshes. In contrast, the FVM in the single mesh simulations is inherently conservative since the cells are connected via shared faces. The error of the mass conservation in the overset mesh simulations could inflict unphysical pressure fluctuation since the pressure correction algorithms applied in the FVM utilize the mass defect to calculate the pressure in incompressible fluid. Consequently, the accuracy of the flow solution could be reduced. The mass conservation has been evaluated in the literature using different approaches. Several studies [19–21] treated the conservation as part of the discretization error and not as a separate issue. These studies utilized methods based on the Richardson extrapolation to evaluate the uncertainty of the simulations. Others have evaluated the mass flow difference between inlet and outlet [22] or compared the L1 or L2 norms of the analytical and simulated quantities [23, 24]. Völkner et al. [16] defined the mass defect as the sum of mass fluxes across overlapping surfaces between interpolated and calculated cells. Chandar [17] approached the issue through the pressure equation derived from the incompressible Navier-Stokes equations and proposed that the mass conservation error could be interpreted as a source or sink term due to the overlapping region. He calculated both L1 and L2 volume-weighted errors between interpolated and exact quantities. In addition, other methods for simulating intermeshing rotors have been proposed, such as the smoothed particle hydrodynamics (SPH) method [25, 26], the immersed solid technique [27] and the added and eliminated mesh method [28].

Various commercial and open-source CFD software are available. One open-source software is the widely used OpenFOAM® which has been applied to simulate various applications with rotating geometries, such as stirred tanks [29–32], bioreactors [33, 34], centrifugal pumps [35, 36], and turbines [37–40]. However, the methods applied for these applications were not suitable for intermeshing rotors and only a few studies use the overset mesh method implemented in OpenFOAM®. Singh Tomar et al. [14] evaluated a mixer with three rotors and studied the heating of a viscous fluid in the mixer. The overset simulation was validated using the well-known case of Taylor-Couette flow between two concentric cylinders and the velocity profile simulated with the overset mesh method was in good accordance with the analytical profile. Casari et al. [41] evaluated suitable methods available in OpenFOAM® for simulating positive displacement machines. They stated that the computational times of the overset mesh method and the remeshing approaches were unacceptable for realistic machines, and the Immersed Boundary Method had issues in solving boundary layers. Therefore, they suggested using body-fitted structured grids for twin screw compressors with intermeshing rotors. However, this method had issues related to mass conservation in 3D simulations even though the simulated results were satisfactory compared to the experimental data in 2D simulation.

Here, the main research focus is on the overset mesh method in OpenFOAM®. Two research gaps were identified based on the literature survey: 1) The mass conservation error has been addressed separately from the discretization error in only a few studies and 2) the intermeshing rotors have been simulated using the overset mesh method only in limited number of studies. The main objectives of the study are: 1) verify the implementation by comparing the concentric cylinder case to the analytical solution, 2) assess the implementation using one six-bladed impeller, 3) demonstrate the functionality of the overset mesh method for two counter-rotating and intermeshing six-bladed impellers, and 4) evaluate the conservation of a transported passive scalar in the intermeshing impellers simulation to highlight the conservation properties of the overset mesh method.

2. Numerical methods

2.1. **Fluid dynamical properties.** In the present study, Newtonian fluid was studied using the properties of water (density $\rho = 1000$ kg/m^3 and kinematic viscosity $\nu = 10^{-6}$ m^2/s).

2.2. **Governing equations.** The governing equations for the simulations were the incompressible Navier-Stokes equations which read as follows [17, 42]:

$$\nabla \cdot \mathbf{U} = 0, \tag{1}$$

$$\frac{\partial}{\partial t}(\mathbf{U}) + \nabla \cdot ((\mathbf{U} - \mathbf{U}_g)\mathbf{U}) = -\nabla p + \nu \nabla^2 \mathbf{U}, \tag{2}$$

where $\mathbf{U}$, $\mathbf{U}_g$, p, and t were the velocity, the velocity of the moving mesh, the kinematic pressure, and time, respectively. In order to determine the velocity of the moving mesh, the space conservation law (integral form) was solved as follows [42] [43, p.330]:

$$\frac{\partial}{\partial t} \int_V dV - \int_S \mathbf{U}_g \cdot \mathbf{n} dS = 0, \tag{3}$$

where V and S were the volume, and the surface of the simulated domain, respectively, and $\mathbf{n}$ was the unit surface normal of the surface. In the OpenFOAM® code, the fluxes are computed using interpolation of the field variables from the cell centroids to the cell faces. The linear systems of the governing equations were solved using `overPimpleDyMFoam` which applied the PIMPLE algorithm utilizing the pressure correction algorithms. [44]

The transportation equation of the passive scalar (c) was as follows:

$$\frac{\partial c}{\partial t} + \nabla \cdot (\mathbf{U}c) - \alpha \nabla^2 c = 0, \tag{4}$$

where α was the diffusivity of the scalar c.

2.3. **Simulation cases.** Figure 1 presents the three simulation cases studied. The two-dimensional simulations were conducted using OpenFOAM® version v2306.

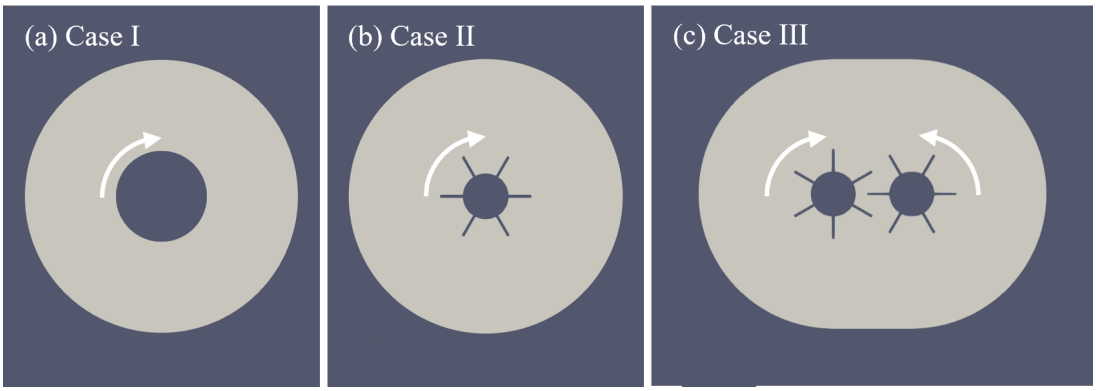

Figure 1. The simulation cases (a) Case I: the concentric cylinders, (b) Case II: one impeller, and (c) Case III: two intermeshing impellers.

In Case I, the well-known case of two concentric cylinders was applied to verify the implementation of the overset mesh method. In this case, the outer cylinder was stationary while the inner cylinder (with diameter D) rotated at a constant angular frequency (ω) such that the Reynolds number was Re = 100. This case was simulated using both the single mesh and the overset mesh methods, and the results were compared to the well-known analytical solution (see the derivation, e.g. by White [45]). The sensitivity of the results to three numerical approaches was investigated including the time discretization scheme, the time step length and the overset interpolation method.

In Case II, one six-bladed impeller (diameter D) in a tank was simulated to assess the implementation of the overset mesh method in OpenFOAM®. Similarly to the first case, the tank wall was stationary while the impeller rotated such that the Reynolds number was Re = 100. Both single and overset mesh methods were applied, and five different mesh topologies were studied.

In Case III, two six-bladed impellers in a tank were simulated to demonstrate the overset mesh implementation in OpenFOAM®. The impellers rotated in opposite directions with the same angular frequency than in the one impeller case. The overset mesh method was only applied for the two impeller simulations since the single mesh method is not suitable for this case. Also, the conservation of a transported passive scalar was evaluated.

2.4. **Meshing approaches.** Two meshing approaches were applied in this work: the single mesh approach and the overset mesh method. The single mesh method was used to obtain reference solutions for cases where single mesh can be used. An illustration of the single mesh is presented in Fig. 2(a) where the added (green color) cylinder indicates a rotating object.

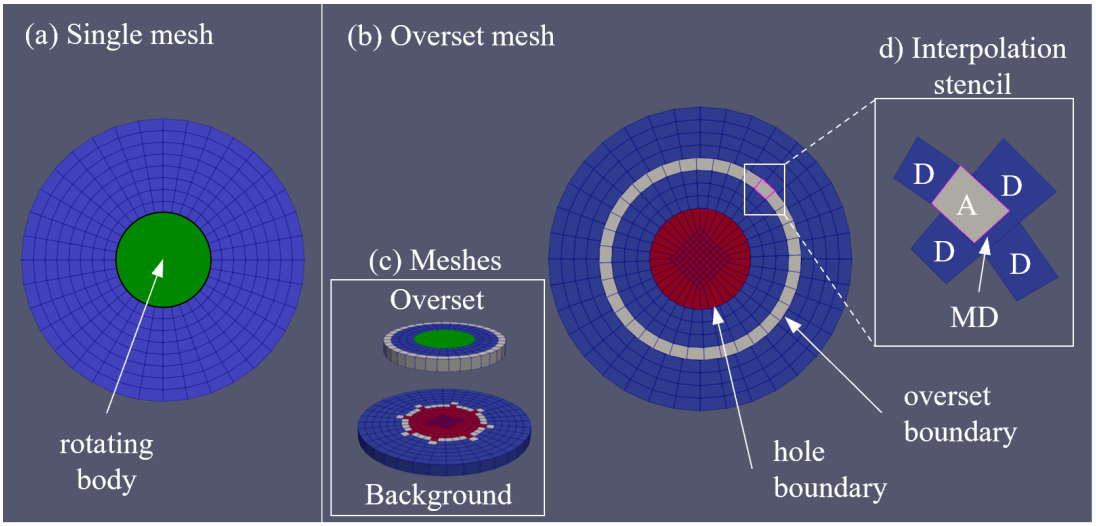

Figure 2. The meshing approaches: (a) a schematic of the single mesh approach, (b) a schematic of the overset mesh method, (c) the overlapping meshes applied in the overset mesh method, and (d) the interpolation stencil for the overset mesh method where the applied abbreviations are as follows: A – acceptor cell, MD – master donor cell, and D – donor cells.

A simplified example of the overset meshes is presented in Fig. 2(c). The overset mesh represented the domain around the rotating object (green-color cylinder in Fig. 2(c) added for clarity) while the background mesh completely covered the simulated domain. Each cell was classified by one of the three cell types: passive, active, or interpolated. The passive cells were inside the boundaries of the solid rotating object and thus, no calculations for the fluid flow were executed in these cells. These cells are marked with a red color in Fig. 2(b)-(d). In the active cells, the linear systems of the discretized governing equations were solved to obtain the field variables similarly to the single mesh method. These cells are marked with a blue color in Fig. 2(b)-(d). In the interpolated cells, the field variables were interpolated from the overlapping mesh. These cells are indicated using a grey color in Fig. 2(b)-(d).

In the overset interpolation, the algorithm started by identifying the acceptor-donor pairs in the interpolation stencil (Fig. 2(d)). First, the interpolated cells were defined adjacent to either the overset boundary or the passive hole cells as presented in Fig. 2(b)-(c). An example of one acceptor cell (A) at the overset mesh is presented in Fig. 2(d). Second, the master donor cell (MD) from the overlapping background mesh was identified. The MD was determined as the cell closest to the acceptor cell and it was found using the global cell numbering. If the cell type of the MD was passive, the cell type of the acceptor cell was automatically changed from interpolated to porous. In porous cells, the field variables were obtained locally, similar to the active cells. Third, the neighboring cells of the MD were assigned as the donor cells (D). This process of defining all the donor cells is called the donor search.

Finally, the field variables, such as velocity and pressure in the acceptor cell, were defined as follows:

$$\phi_{acceptor} = \sum w_i \phi_{donor,i}, \tag{5}$$

where $\phi_{acceptor}$ and $\phi_{donor,i}$ were the field variable value in the acceptor and donor cells, respectively. The interpolation scheme of the field variables was embedded into the sparse linear system of equations i.e. Eqn. 5 is solved implicitly. The weights w_i were calculated using the distances between the centers of the

acceptor and the donor cells according to the applied overset interpolation scheme. Here, two schemes were applied:

- Inverse distance method (invD)

$$w_i = \frac{\frac{1}{|d_i|}}{\sum \frac{1}{|d_i|}} \tag{6}$$

- Least squares method (LS)

$$w_i = \frac{\frac{1}{|d_i|^2} - \left(\frac{M_{i,x}}{|d_i|^2} \sum \frac{d_{i,x}}{|d_i|^2} + \frac{M_{i,y}}{|d_i|^2} \sum \frac{d_{i,y}}{|d_i|^2} + \frac{M_{i,z}}{|d_i|^2} \sum \frac{d_{i,z}}{|d_i|^2} \right)}{\sum \frac{1}{|d_i|^2} - \sum \left(\frac{M_{i,x}}{|d_i|^2} \sum \frac{d_{i,x}}{|d_i|^2} + \frac{M_{i,y}}{|d_i|^2} \sum \frac{d_{i,y}}{|d_i|^2} + \frac{M_{i,z}}{|d_i|^2} \sum \frac{d_{i,z}}{|d_i|^2} \right)} \tag{7}$$

where d_i was the distance between the cell centers of the acceptor and the donor cells. $M = (A^T A)^{-1} A^T$ was a matrix calculated using all the donor cells $A = \left[\frac{d_{i,x}}{|d_i|^2} \quad \frac{d_{i,y}}{|d_i|^2} \quad \frac{d_{i,z}}{|d_i|^2} \right]$. The pseudo-inverse $(A^T A)^{-1}$ was calculated using the singular value decomposition.

3. Numerical set-up

3.1. **Standard simulation set-up for each simulation case.** In the standard simulation set-up, time was discretized using the backward differencing scheme. As a remark, it is a common practice in CFD simulations to prefer at least second-order time and space discretization methods in transient simulations. The time step was adjusted automatically such that the maximum Courant number $Co_{max} = \Delta t \mathbf{U}/\Delta x$ was 0.5 to ensure that the fluid particle did not move through the cell during one time step ($Co < 1$) and thus, to improve the transient accuracy. The divergence term of the velocity was discretized using Gaussian integration with linear interpolation. The default discretization schemes were applied for the gradient terms (Gaussian integration with linear interpolation) and the Laplacian terms (Gaussian integration with linear interpolation scheme for the diffusion coefficient and corrected scheme for the surface normal gradient). For the overset interpolation, the second-order least squares method was applied in Case I but in the impeller cases, the first-order inverse distance method was applied to increase the numerical stability. The applied boundary conditions for the different simulation cases are summarized in Fig. 3. For the pressure boundary condition in Cases II and III, a reference pressure was applied on the outer edge instead of on only a single reference point due to issues in the numerical stability (see Chapter 4.4).

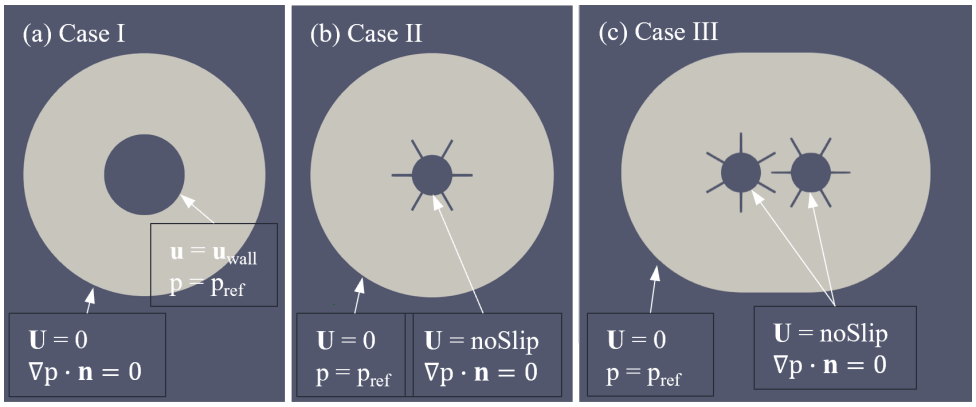

Figure 3. The applied boundary conditions for the different simulation cases. The abbreviations are as follows: **U** – velocity, p – pressure, **n** – surface normal vector.

3.2. **Case I: sensitivity to numerical approaches.** In Case I, the sensitivity of the results to three numerical approaches was investigated. In the first approach, the time discretization scheme was changed from the second-order backward differencing scheme to the first-order implicit Euler scheme. In the second approach, the time step sensitivity was investigated by decreasing the maximum Courant number from 0.5 to 0.25. In the third approach, the overset interpolation was calculated using the first-order inverse distance method instead of the second-order least squares method. The reference simulation case was solved using the single mesh method. These numerical approaches are summarized in Tab. 1.

Table 1. The sensitivity of the results to the following numerical approaches was studied in Case I. The abbreviations are as follows: invD – inverse distance method, LS – least squares method.

Numerical approach	Simulation method	Time discretization scheme	Maximum Courant Number	Overset interpolation scheme
Reference	**single**	backward	0.50	LS
Standard	**overset**	backward	0.50	LS
Time scheme	overset	**Euler**	0.50	LS
Timestep	overset	backward	**0.25**	LS
Interpolation	overset	backward	0.50	**invD**

3.3. **Case II: sensitivity to mesh topologies.** In Case II, the sensitivity of the results to different mesh topologies was tested to estimate how the location of the overset interpolation affected the results. The tested meshing options are presented in Fig. 4. In terms of the overset mesh, three different topologies were tested: 1) a circular mesh with a large diameter (D_{large}), 2) a circular mesh with a small diameter (D_{small}), and 3) a conformal mesh where the overset mesh boundary followed closely the impeller shape. The first topology (D_{large}) was applied in Meshes 1 and 2 presented in Fig. 4(a)-(b). This mesh extended the overset interpolation to region where the gradients of the field variables in the interpolated cells were smaller than when using the other topologies. In the second topology (D_{small}), these gradients were increased (Meshes 3 and 4 in Fig. 4(c)-(d)) and the third topology – using the conformal mesh – increased these gradients even further (Mesh 5 in Fig. 4(e)). In terms of the background mesh, the large passive area (A_{large}) extended the overset interpolation to a region with smaller gradients of field variables (Meshes 1 and 3 in Fig. 4(a) and (c)) compared to the small passive area (A_{small} Meshes 2, 4 and 5 in Fig. 4 (b), (d) and (e)). For the conformal mesh around the impeller, mesh refinement on the background mesh was required in the region where the meshes overlapped to ensure that the interpolated cells of the background mesh had donor cells available from the overset mesh. In addition, the effect of the overset interpolation method was tested using the Meshes 1 and 2. The reference simulation was obtained using the single mesh method where the rotating impeller was simulated utilized the multiple reference frames (MRF) (see e.g. Patil et al. [46]).

3.4. **Case III: sensitivity mesh topologies and conservation of transported scalar.** In Case III, the functionality of the overset mesh method for simulating two intermeshing impellers was demonstrated. The suitability of different mesh topologies was investigated by studying two mesh topologies presented in Fig. 5: a) the large circular overset mesh with small passive area at the background mesh as well and b) the conformal overset mesh.

The conservation of a passive scalar was evaluated to understand how accurately the scalar was conserved when the overset mesh method was applied. The value of the scalar was initially 0 on the left side of the tank and 1 on the right side. The convection equation for the scalar was solved using three different divergence schemes: the standard Van Leer scheme (`vanLeer`) and its bounded version where the scalar was bounded between 0 and 1 (`vanLeer01`) were tested. Also, the bounded version of the gamma NVD (normalized variable diagram) scheme [47] (`Gamma01`) was applied in the numerical tests. The diffusion term of the transport function was omitted, and the number of the correctors was set to 2.

3.5. **Metrics of the functionality.** In the first metric, the mass conservation was estimated using the mass conservation errors. The global mass conservation error (ε) and the error using the absolute value of the velocity divergence i.e. L1 error (ε_{L1}) were calculated based on the mass conservation law as follows:

$$\varepsilon = \left| \frac{\sum (\nabla \cdot \mathbf{U})_i dA_i}{\sum dA_i} \right|, \tag{8}$$

$$\varepsilon_{L1} = \frac{\sum |(\nabla \cdot \mathbf{U})_i| dA_i}{\sum dA_i}, \tag{9}$$

where $\mathbf{U}$ and A were the velocity and the cell area, respectively. Only the active cells were included in the calculation of ε and ε_{L1}. The error was normalized by the representative velocity gradient ($\mathbf{U}/\Delta x$) where $\mathbf{U}$ and Δx were the representative velocity and the corresponding cell size, respectively. The representative velocity was the tangential velocity of the rotating cylinder or the impeller tip. The

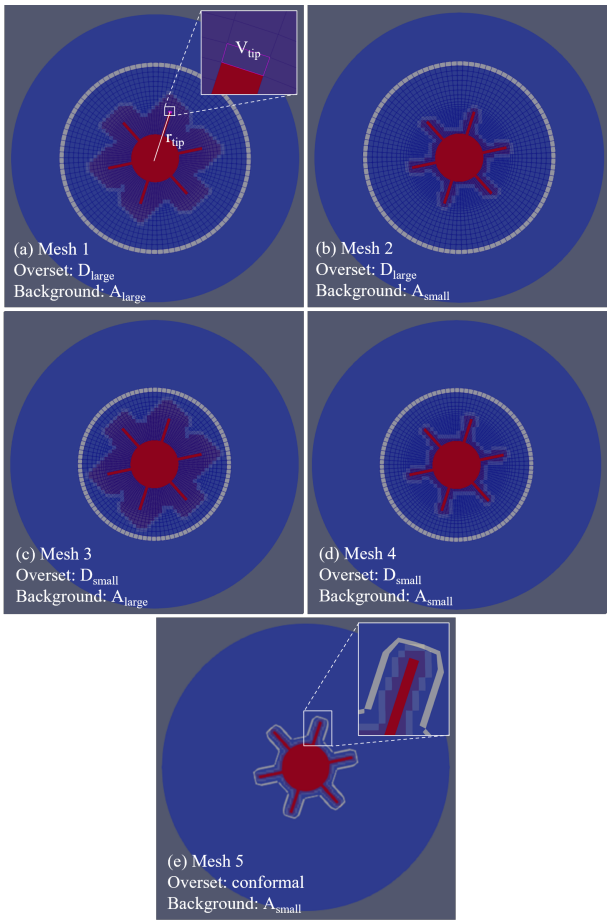

Figure 4. The different mesh topologies investigated in Case II. The abbreviations are as follows: D_{large} – large circular overset mesh, D_{small} – small circular overset mesh, conformal – conformal overset mesh, A_{large} – large passive area at background mesh, and A_{small} – small passive area at background mesh.

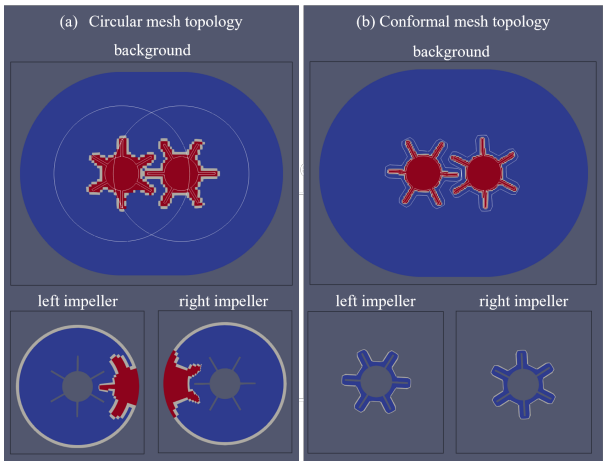

Figure 5. The different mesh topologies investigated in Case III.

corresponding cell size ($\Delta x = \sqrt{A_{cell}}$) was obtained from the cell adjacent to the rotating cylinder or the impeller tip. The means and standard deviations of ε and ε_{L1} were calculated at the steady state conditions.

In the second metric, the dimensionless power number describing the ratio between the power resistance to the inertial forces was studied. It accounted the effect of the pressure and viscous forces and thus, it

could estimate the oscillation in the pressure and velocity fields. The power number was calculated as follows:

$$N_p = \frac{P}{\rho N^3 D^5}, \tag{10}$$

where P was the power (absolute value applied in this work), ρ was the density of the fluid, N was the rotational speed ($N = \omega/(2\pi)$), and D was the diameter of the rotating cylinder or the impeller. The power (P) was calculated based on the torque (Γ) as $P = 2\pi N\Gamma = \omega\Gamma$ where the torque was obtained from the rotating cylinder or impeller wall. The mean and the standard deviation of the power number were calculated at the steady state which was presumed as the simulation period where the mean power number remained essentially constant.

In the third metric, the velocity profiles obtained from the overset mesh simulations were compared to the reference profiles to estimate the accuracy of the overset mesh method. The profiles were obtained along the selected lines as presented in Fig. 6. The velocity profiles were normalized by the tangential velocity of the rotating cylinder or the impeller tip.

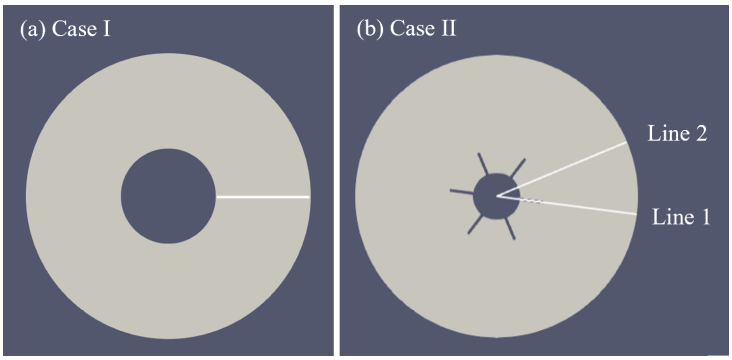

Figure 6. The locations where the velocity profiles were obtained for (a) Case I and (b) Case II.

4. **Results and discussion**

The mesh independence study for each simulation case is provided in the Appendix A. In line with the objectives of the study, this section aims at verifying the implementation of the overset mesh method by comparing the concentric cylinder case to the analytical solution, assessing the implementation using one six-bladed impeller, demonstrating the functionality of the overset mesh method for two counter-rotating and intermeshing six-bladed impellers, and evaluating the conservation of a transported passive scalar in the intermeshing impellers simulation. An approximation of the simulation time could be interesting to industrial applications. To simulate one rotation of the Case I in serial, the simulation time of the reference case was ∼1 second while the overset simulations lasted closer to ∼1 minute using a personal computer. Regarding one rotation of the Case II, the execution time for the reference case was ∼2 s while the overset simulations using circular and conformal meshes were approximately ∼5 min and ∼50 min, respectively. For the Case III, the CSC supercomputer Puhti with single core (please see more details in [48]) was utilized and the time to execute one rotation was significantly longer (∼ 10 - 100h) on a single processor depending on the solver settings.

4.1. **Case I.** The velocity profiles of the different numerical approaches are presented in Fig. 7. The reference profile obtained utilizing the single mesh method corresponded with the analytical solution accurately. For the overset simulation, the profiles obtained from all the numerical approaches were essentially reproducing the analytical velocity profile. The velocity profiles were not sensitive to the different numerical approaches.

In Fig. 8, a representative graph of the steady state velocity field is presented in Fig. 8(a), and the normalized divergences of the velocity are illustrated for the single mesh simulation in Fig. 8(b) and for the overset mesh simulation in Fig. 8(c)-(d). In this example, the standard numerical approached was applied. The maximum and minimum divergences were located close to the rotating cylinder for both the single mesh simulation and the overset mesh of the overset mesh simulation. In the background mesh of the overset mesh simulation, the maximum and minimum divergences were found in a few interpolated and passive cells.

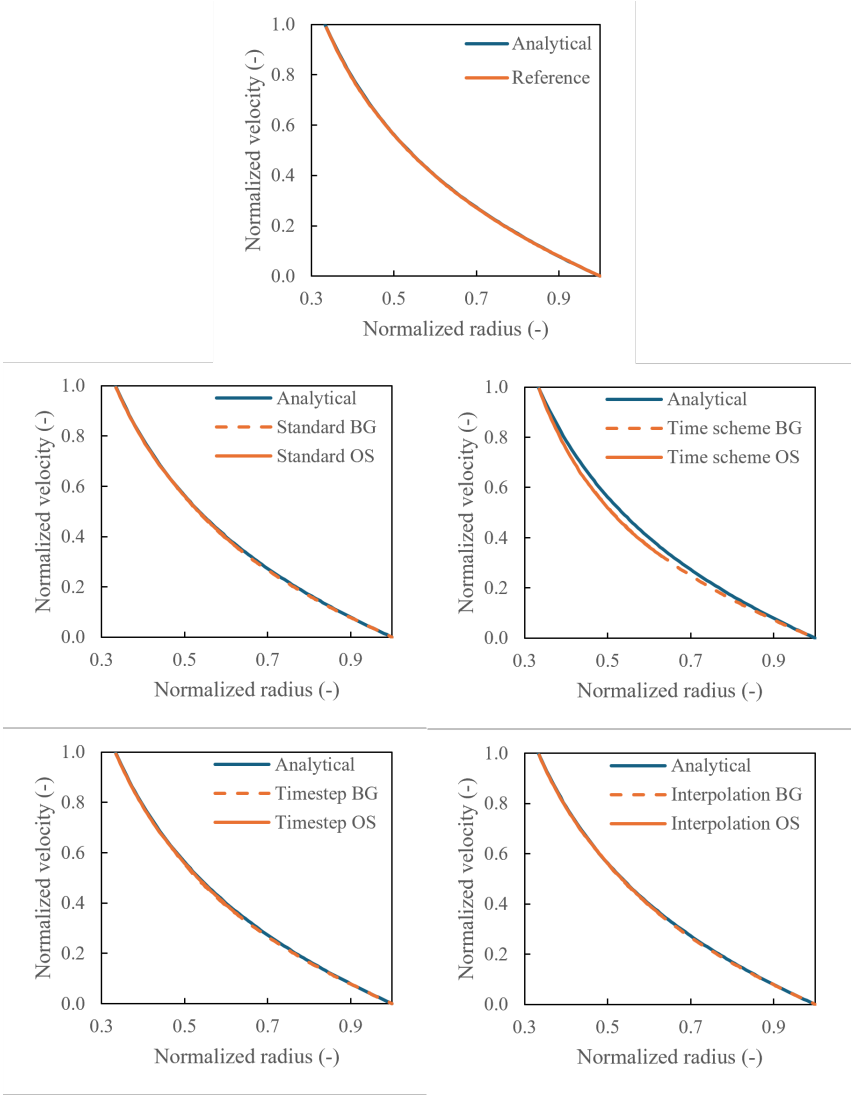

Figure 7. Case I: The effect of the different numerical approaches on the velocity profiles (normalized by the tangential velocity of the rotating cylinder). The approaches are summarized in Tab. 1. The abbreviations are as follows: BG - background mesh, OS - overset mesh.

In Tab. 2, ε and ε_{L1} obtained from the different numerical approaches are summarized. The ε and ε_{L1} were not sensitive to the different numerical approaches, but some fluctuation was observed when the overset interpolation was changed from the LS to the invD (Interpolation).

Table 2. Case I: The conservation errors ε and ε_{L1}.

Numerical approach	ε (-)	ε_{L1} (-)
Reference	$4.1 \cdot 10^{-13} \pm 2.9 \cdot 10^{-13}$	$5.9 \cdot 10^{-5} \pm 2.0 \cdot 10^{-9}$
Standard	$8.7 \cdot 10^{-6} \pm 1.4 \cdot 10^{-6}$	$9.4 \cdot 10^{-5} \pm 1.4 \cdot 10^{-5}$
Time scheme	$4.0 \cdot 10^{-6} \pm 9.1 \cdot 10^{-7}$	$7.7 \cdot 10^{-5} \pm 1.1 \cdot 10^{-5}$
Time step	$1.0 \cdot 10^{-5} \pm 2.0 \cdot 10^{-6}$	$9.6 \cdot 10^{-5} \pm 1.6 \cdot 10^{-5}$
Interpolation	$5.3 \cdot 10^{-5} \pm 2.7 \cdot 10^{-5}$	$1.5 \cdot 10^{-4} \pm 3.8 \cdot 10^{-5}$

In Fig. 9, the analytical $N_p = 43.8$ is presented along with N_p obtained using the different numerical approaches. No pressure fluctuation was observed in N_p due to the applied boundary conditions and N_p was utilized to assess the sensitivity of the different numerical approaches. The reference case simulated using the single mesh method corresponded well with the analytical solution. The overset simulations

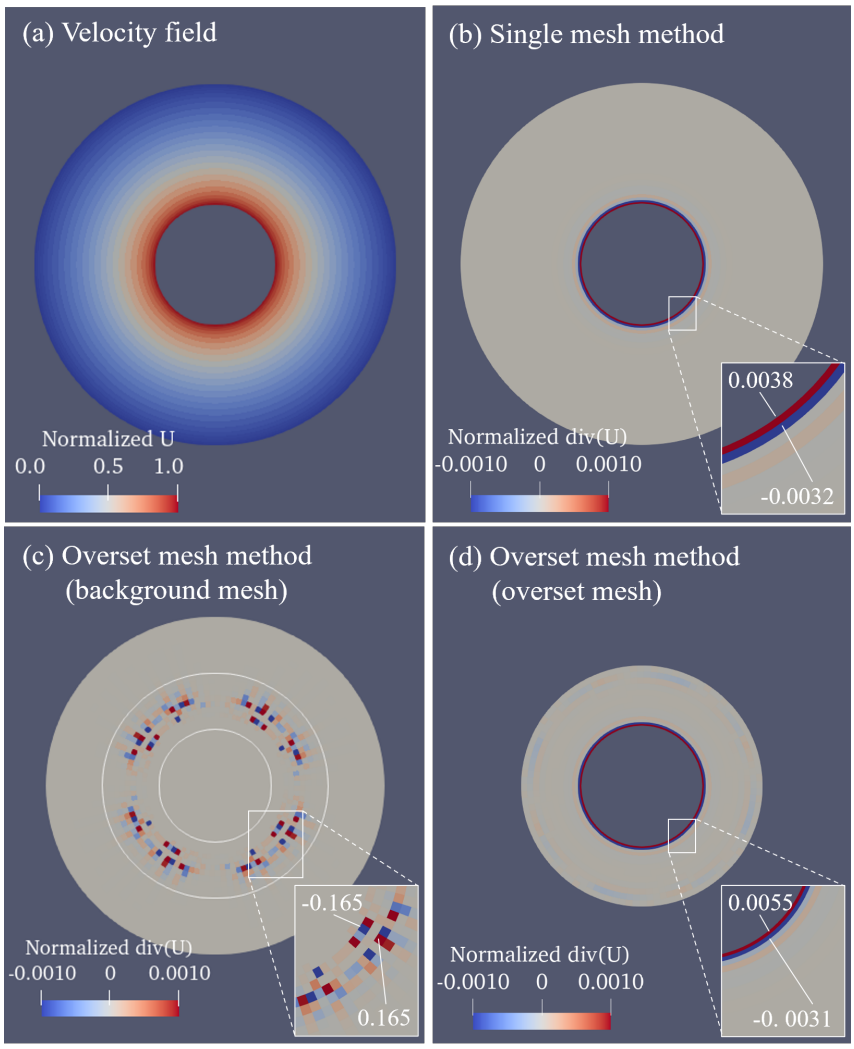

Figure 8. Case I: (a) the normalized velocity field as well as the normalized divergence of velocity for (b) the single mesh simulation, (c) the overset mesh simulation (background mesh) and (d) the overset mesh simulation (overset mesh). The peak values of the velocity divergence are highlighted. The velocity was normalized by the tangential velocity of the rotating cylinder and the divergence by representative velocity gradient ($U_{cylinder}/\Delta x_{innerBoundary}$).

were the most sensitive to the time discretization scheme (Time scheme in Fig. 9) while other approaches estimated N_p accurately compared to the analytical solution.

The reference simulation utilizing single mesh method matched exceptionally well with the analytical solution. Therefore, such single mesh simulations could serve as useful reference cases in more complex impeller simulations where analytical solutions are not available. The overset mesh simulations were the most sensitive to the time discretization scheme and therefore, the second-order scheme (backward differencing) was applied in the impeller simulations.

4.2. **Case II.** In Fig. 10, the velocity profiles are presented at the steady state conditions. It was noted that the resulting velocity profiles were not sensitive to the mesh topologies.

In Fig. 11, a representative graph of the steady state velocity is provided for the single mesh simulation (a) as well as the divergence of the velocity for the single mesh simulation (b) and the overset mesh simulation (c)-(d). In this example, the conformal mesh was applied. The maximum and minimum divergences were found close to the tip of the blade for the single mesh simulation. In the overset mesh simulations, the maximum and minimum divergences on the background mesh were found in a few passive cells while the maximum and minimum divergences on the overset mesh were located near the interpolation boundary.

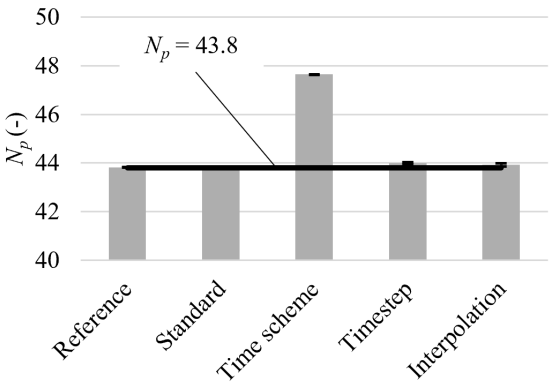

Figure 9. Case I: The effect of the different numerical approaches on N_p. The approaches are summarized in Tab. 1.

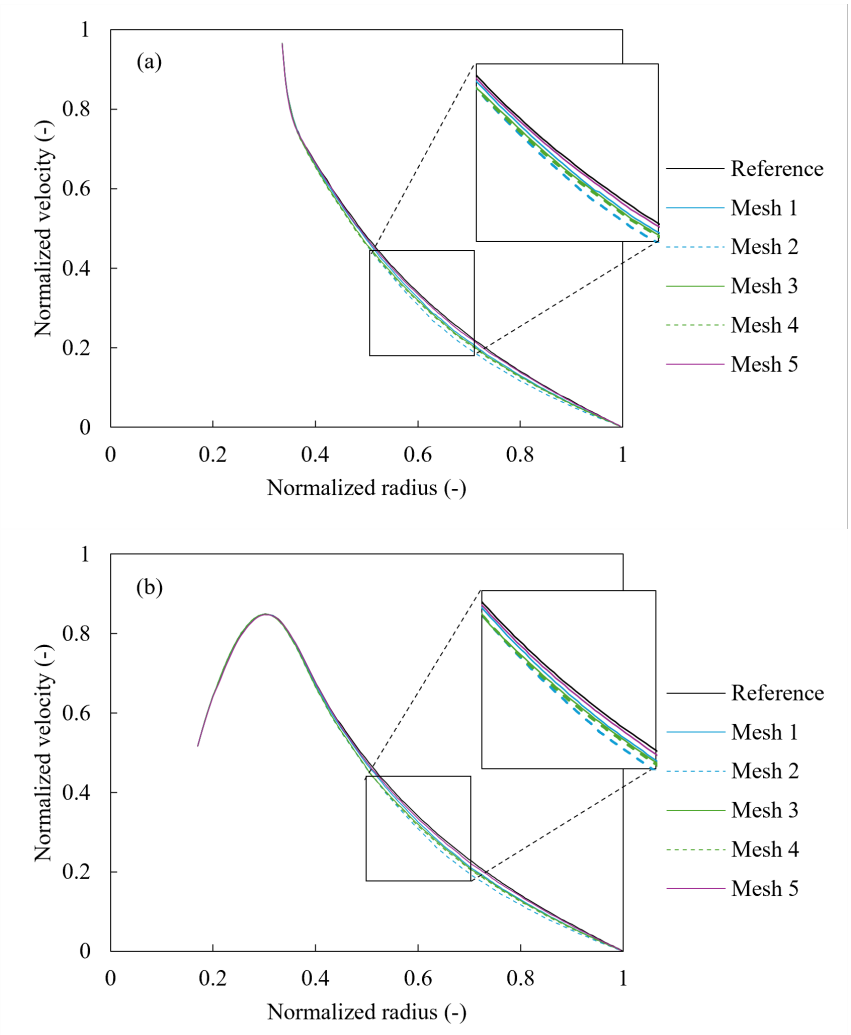

Figure 10. Case II: The effect of the different mesh topologies on the velocity profiles (normalized by the tip velocity of the blade) over (a) Line 1, and (b) Line 2 presented in Fig. 6. The topologies are illustrated in Fig. 4.

In Tab. 3 , ε and ε_{L1} obtained from the different mesh topologies are summarized. In terms of ε, all circular mesh topologies (Meshes 1-4) had the same order of magnitude and ε was the lowest when the conformal mesh (Mesh 5) was used. One potential reason was that the mesh refinement was required on

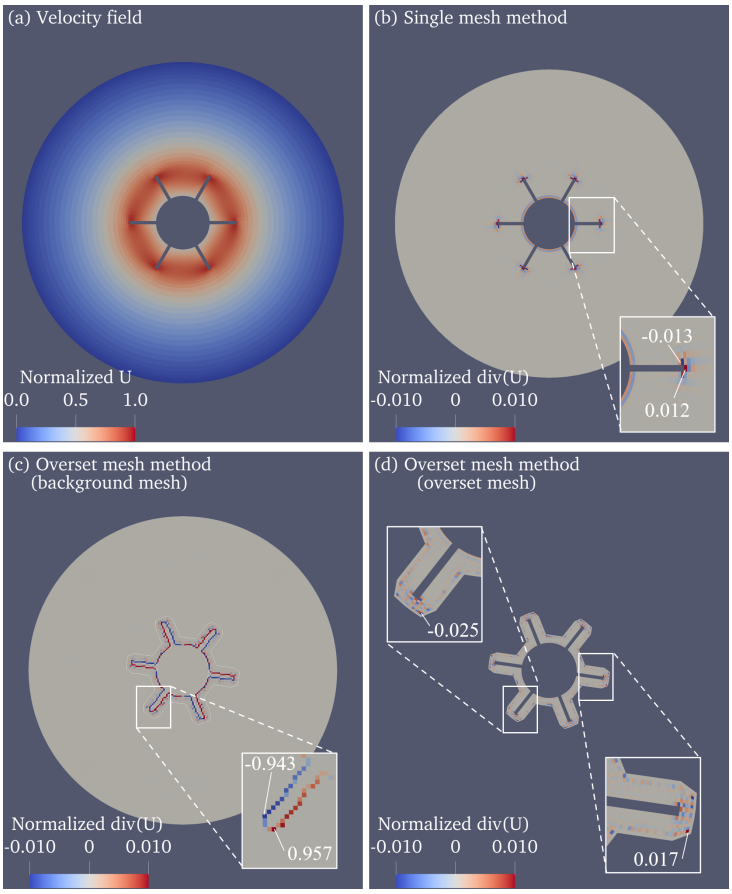

Figure 11. Case II: (a) the normalized velocity field as well as the normalized divergence of velocity for (b) the single mesh simulation, (c) the overset mesh simulation (background mesh) and (d) the overset mesh simulation (overset mesh). The peak values of the velocity divergence are highlighted. The velocity was normalized by the tip velocity of the blade and the divergence by the representative velocity gradient ($U_{tip}/\Delta x_{tip}$).

the background mesh due to the overset interpolation and the mesh refinement typically improves the accuracy of the simulations. The ε_{L1} was not sensitive to the mesh topology.

Table 3. Case II: The conservation errors ε and ε_{L1}. The topologies are illustrated in Fig. 4.

Numerical approach	ε (-)	ε_{L1} (-)
Reference	$6.4 \cdot 10^{-13} \pm 3.5 \cdot 10^{-13}$	$7.4 \cdot 10^{-5} \pm 9.4 \cdot 10^{-10}$
Mesh 1	$1.3 \cdot 10^{-5} \pm 1.7 \cdot 10^{-5}$	$2.0 \cdot 10^{-4} \pm 3.7 \cdot 10^{-5}$
Mesh 2	$1.4 \cdot 10^{-5} \pm 5.2 \cdot 10^{-6}$	$2.1 \cdot 10^{-4} \pm 9.1 \cdot 10^{-6}$
Mesh 3	$1.3 \cdot 10^{-5} \pm 8.8 \cdot 10^{-6}$	$2.2 \cdot 10^{-4} \pm 1.3 \cdot 10^{-5}$
Mesh 4	$1.3 \cdot 10^{-5} \pm 6.6 \cdot 10^{-6}$	$2.1 \cdot 10^{-4} \pm 5.5 \cdot 10^{-6}$
Mesh 5	$2.3 \cdot 10^{-6} \pm 1.7 \cdot 10^{-6}$	$1.1 \cdot 10^{-4} \pm 4.3 \cdot 10^{-6}$

In Fig. 12, the N_p obtained using the different mesh topologies are presented. The reference $N_p = 9.0$ was obtained from the simulation utilizing the single mesh method. It was noted that the N_p obtained from the overset simulations was sensitive to the mesh topologies. When the circular meshes (Meshes 1-4) were applied, the N_p obtained from the overset mesh simulations were in accordance with the reference case. In contrast, N_p was overestimated when the conformal mesh (Mesh 5) was applied. The accuracy was increased to accepted level when the conformal mesh was refined such that the interpolated cells at overset and background meshes did not overlap. The pressure fluctuation was estimated by studying the standard deviation in the pressure component of N_p. The fluctuation was insignificant when the circular meshes (Meshes 1-4) were considered. Regarding the conformal mesh, fluctuation was observed

but refining the mesh decreased also the fluctuation. In addition, the overset interpolation method did not influence the accuracy of N_p.

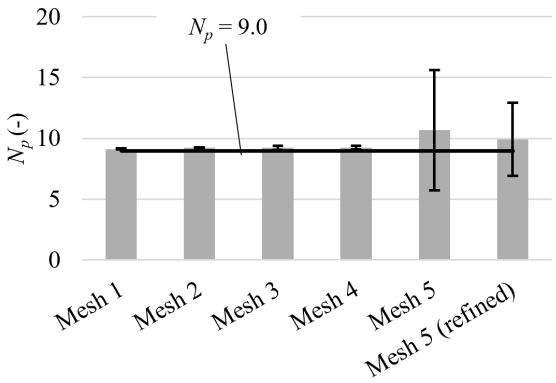

Figure 12. Case II: The effect of the different mesh topologies on N_p. The topologies are illustrated in Fig. 4. Please note the high N_p fluctuation for Mesh 5 i.e. the conformal mesh topology.

The simulated velocity profiles and N_p matched well with the reference cases. Therefore, it was expected that the acceptable order of magnitude for the errors ε and ε_{L1} were in the range $\sim 10^{-6} - 10^{-4}$.

4.3. **Case III.** The suitability of the circular and conformal mesh topologies was evaluated for the inter-meshing impellers. When the circular meshes were applied around the impellers, few of the interpolated cells were replaced with the porous cells. These porous cells are marked with red in Fig. 13(a). However, the porous cells are not supported for the simulation cases where two inset meshes are on top of the background mesh such as the case simulated here. Therefore, the only meshing topology suitable for Case III was the conformal mesh around the impellers as presented in Fig. 13. In the present study, we did not use the circular meshes in Case III due to the appearance of porous cells and only the conformal mesh topology was applied.

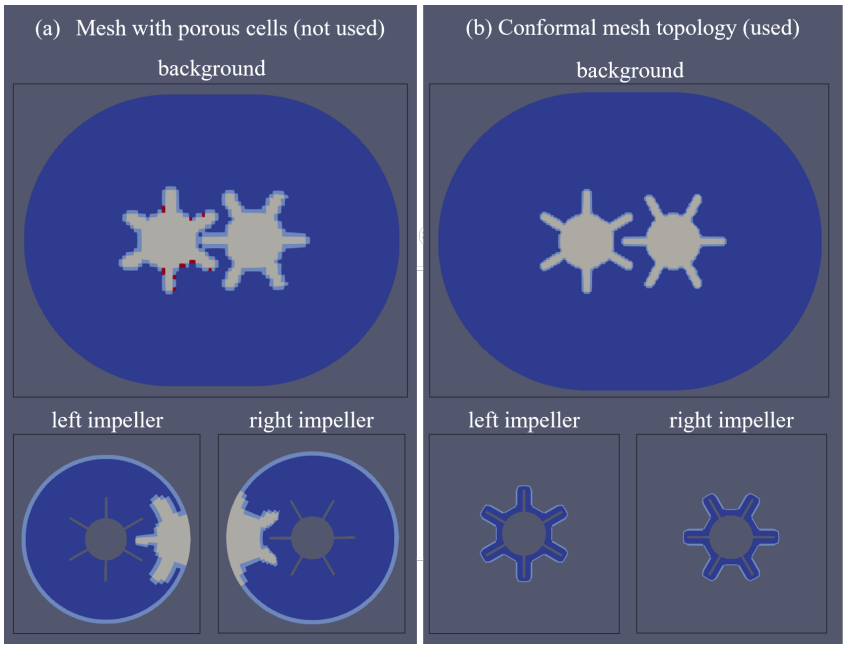

Figure 13. (a) the mesh with porous cells (not used for the simulation of Case III) and (b) the conformal mesh topology (used for the simulation of Case III). The cell types are indicated as follows: active cells (blue), interpolated (light blue), passive (grey) and porous (red).

The normalized divergences of the velocity are presented in Fig. 14 for the background mesh (a) as well as for the left (b) and right (c) impellers. The maximum and minimum divergences in all meshes were found at a few interpolated cells and passive cells similarly to Case II.

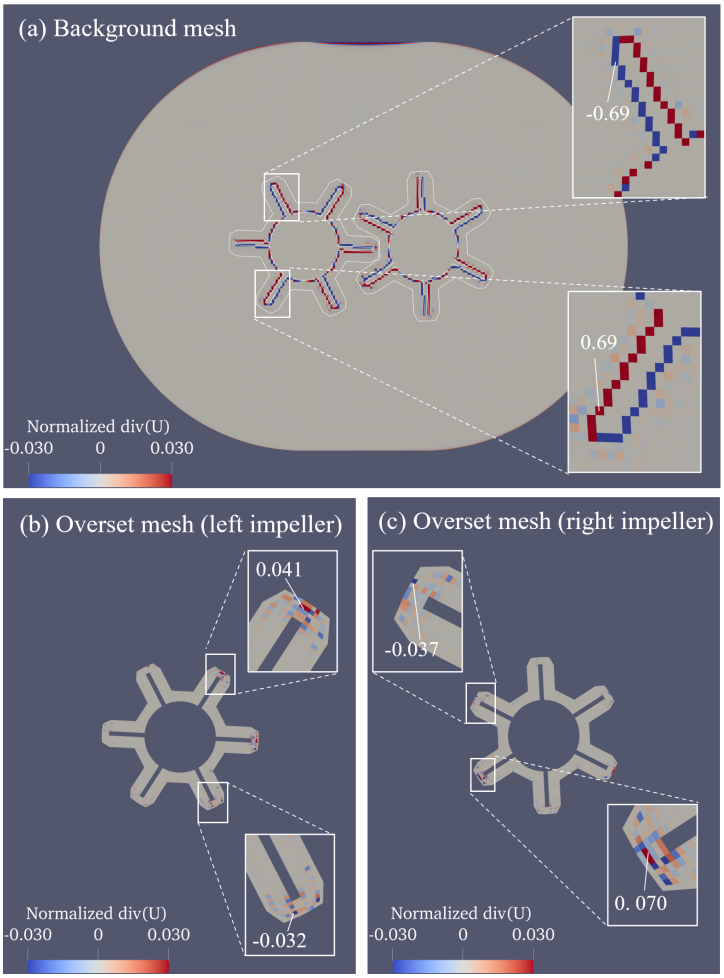

Figure 14. Case III: The normalized divergence of velocity for (a) the background mesh, (b) the left impeller mesh, and (c) the right impeller mesh. The peak values of the velocity divergence are highlighted. The velocity was normalized by the tip velocity of the blade and the divergence by the representative velocity gradient ($U_{tip}/\Delta x_{tip}$).

The conservation errors ε and ε_{L1} were $5.2 \cdot 10^{-6} \pm 4.4 \cdot 10^{-6}$ and $3.9 \cdot 10^{-4} \pm 1.4 \cdot 10^{-5}$, respectively. They were in the same range as for Case II and thus, it was assumed that the mass conservation was at an acceptable level. The N_p values obtained for the right and left impeller were 31.3 ± 34.0 and 31.9 ± 34.2, respectively. The standard deviations of the N_p for both impellers were high, but phenomenologically, we expected that some of this fluctuation was of physical origin. We note that a reliable reference result without overset mesh method is lacking in Case III. In the literature, several researchers have studied intermeshing rotors in the context of kneaders and TSEs [4–8] even though the geometries matching our simulations were not found. These studies utilized FEM and MTS for 3D simulations. However, possible phenomenological pressure oscillation was not discussed. Singh Tomar et al. [14] studied a mixer utilizing a 2D simulation and conformal meshes but they did not report any pressure fluctuation. On the other hand, Chandar [17] studied a 2D simulation of an oscillating cylinder in a closed tank. He stated that such simulations are challenging since there is no mass flow in or out of the system and noted that the drag coefficient was highly oscillatory. In our Case II with one impeller, no physical pressure oscillation was expected. Indeed, the viscous component of N_p was constant for all studied meshes. For Case III with two impellers, the viscous and pressure components of N_p are presented in Fig. 15 and Fig. 16, respectively. The viscous N_p exhibited periodic oscillation which could be of physical origin. The maximum and minimum values of the viscous N_p were observed when one blade of the right and left impeller, respectively, were approaching vertical position in the intermeshing region. A similar periodic

behaviour was noted also for the pressure N_p. However, we observed also some additional unsteady fluctuation which could be caused by the overset interpolation and the conformal mesh topology (see standard deviations in Fig. 12).

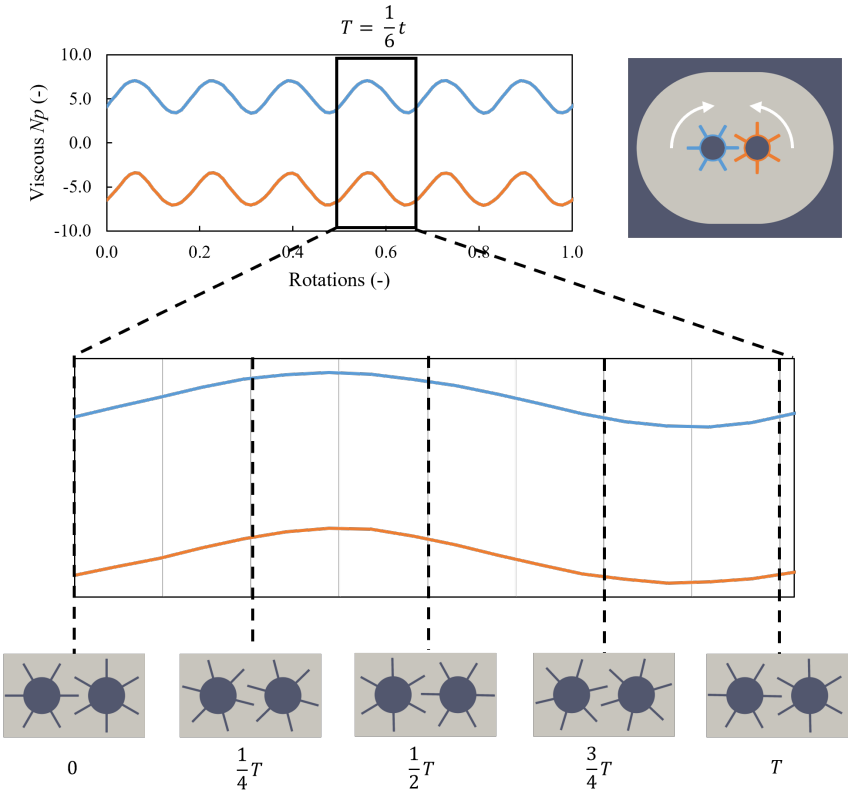

Figure 15. Case III: viscous component of N_P. The abbreviations are as follows: t - time for one rotation, T - period time.

As a final example, the transport of a passive scalar is presented in Fig. 17 at three instants of time using the van Leer scheme. The scalar fields appeared very similar for all the studied schemes. After ten rotations, the normalized scalar average (c_{ave}) for the `vanLeer`, `vanLeer01` and `Gamma01` schemes were 0.9995 ± 0.0005, 0.9995 ± 0.0005, and 0.9994 ± 0.0004, respectively, i.e. the scalar was essentially conserved.

4.4. **Challenges related to the overset mesh method.** The pressure boundary conditions were found to be challenging for the overset mesh method in the impeller simulations (Cases II and III). Since the impeller was considered as an impermeable wall, the Neumann pressure condition (fixed gradient) was applied at the impeller boundary. When the Neumann pressure condition was applied also at the outer wall of the tank, the pressure value in the simulation domain was fixed only at one individual pressure reference point. This caused no stability issues in the single mesh simulation. However, in the overset mesh simulation, the unphysical pressure fluctuation was observed, and the conservation error due to the overset interpolation accumulated around the pressure reference point. The same phenomenon has also been noted e.g. by Chandar [17]. To stabilize the simulations, the pressure at the tank wall was determined using the Dirichlet condition (fixed reference value). In three-dimensional simulations, a reference pressure is typically assigned at the inlet or outlet boundary and thus, the Neumann pressure condition could be assigned to other walls to simulate their physical conditions more realistic.

Another challenge for the overset mesh method was related to the circular overset meshes that overlapped in the two impeller case (Case III). The circular meshes could have been more accurate than the conformal mesh based on the sensitivity comparison of the mesh topologies in the one impeller case (Case II). However, the circular meshes could not be utilized in the simulation where two overset meshes overlapped on top of the background mesh due to the mesh hierarchy algorithm. Therefore, the conformal mesh topology was the only option for simulating the intermeshing impellers. A few algorithmic modifications could be useful for future research to allow the use of circular mesh topology. First, the overset mesh algorithm could support also the overlapping of two meshes on top of the background mesh.

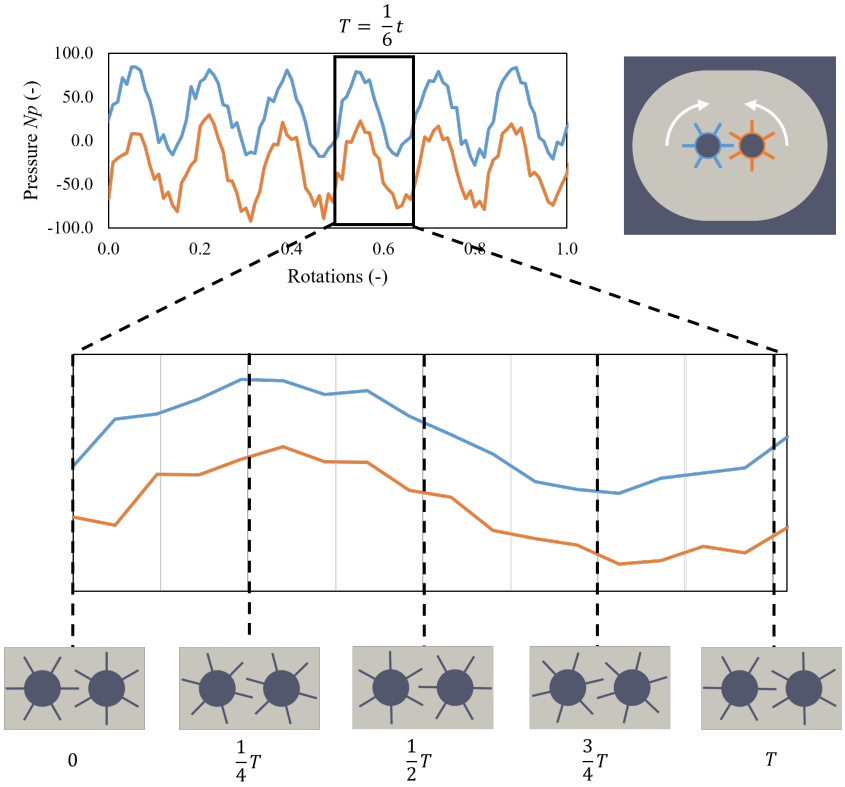

Figure 16. Case III: pressure component of N_P. The abbreviations are as follows: t - time for one rotation, T - period time.

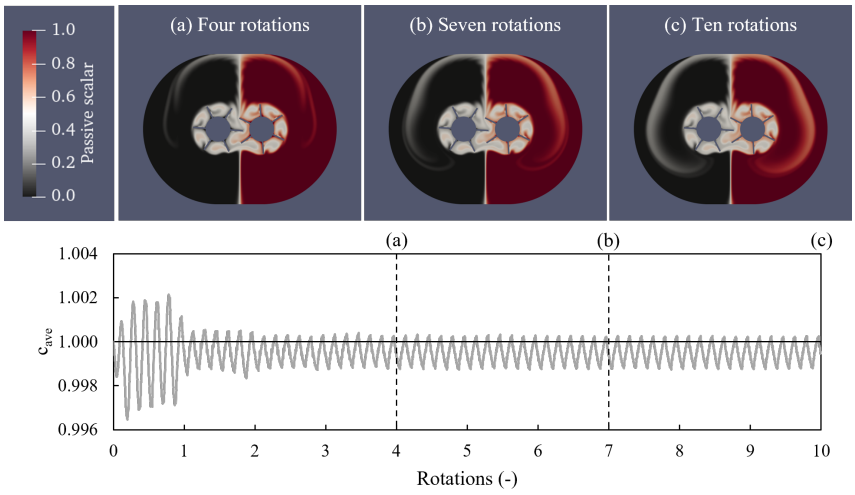

Figure 17. The passive scalar fields after a) four rotations, b) seven rotations, and c) ten rotations as well as the temporal evolution of the normalized scalar average (c_{ave}) using the van Leer scheme.

Second, the mesh hierarchy algorithm could be modified such that the background mesh could interpolate also from the mesh further in the hierarchy and not only from the mesh at the closest hierarchy level. This could facilitate the use of circular meshes around the impeller and improve the mass conservation. Consequently, the unphysical pressure fluctuation could be decrease and the accuracy of the overset mesh simulations could be improved.

5. Conclusion

In this study the main research focus was on the overset mesh method implemented in the open-source CFD software OpenFOAM® and its functionality for simulating intermeshing impellers. The main conclusions of the study were:

1) The simulated results of the concentric cylinders were the most sensitive to the applied time discretization scheme. The length of the time step and the overset interpolation scheme had less effect on the accuracy of the velocity and N_p.

2) The velocity profiles of the one impeller simulations were not sensitive to the studied mesh topologies. In contrast, pressure fluctuation and deviation of the N_p from the reference value were observed when the conformal mesh topology was applied. The mesh refinement improved these issues. The acceptable order of magnitude for the errors ε and ε_{L1} were in the range 10^{-6} and 10^{-4}, respectively.

3) The conformal mesh topology was applied for the simulation of the intermeshing impellers due to the restrictions of the implemented overset mesh algorithm. The conservation errors ε and ε_{L1} were in the same range as in the one impeller simulations but pressure fluctuation was noted indicating possible unphysical fluctuation.

4) Despite the unphysical pressure fluctuation in the simulation of the intermeshing impellers, the transported passive scalar was conserved during the simulations.

It was concluded that the overset mesh method could be applied in one impeller simulations when the proper mesh topology is applied. In the simulation of the intermeshing impellers, the overset mesh method may also be applicable while keeping in mind the possibility of pressure fluctuations.

Acknowledgements

The authors wish to acknowledge CSC – IT Center for Science, Finland, for computational resources.

M.N. is grateful to Professor Jari Hyttinen at Tampere University, and Professor Emeritus Timo Siikonen and M.Sc. (Eng) Esa Salminen from Elomatic Oy (Finland) for fruitful discussion.

This research was funded by the Doctoral School of Industry Innovations (DSII) at Tampere University.

Author Contributions: Conceptualisation, M.N., V.V., M.Ka., R.S. and M.Ke.; methodology, M.N., V.V., M.Ka.; software, M.N.; validation, M.N.; formal analysis, M.N.; investigation, M.N.; resources, M.Ke.; data curation, M.N.; writing—original draft preparation, M.N.; writing—review and editing, M.N., V.V., M.Ka., R.S. and M.Ke.; visualisation, M.N.; supervision, V.V., M.Ka., R.S. and M.Ke.; project administration, R.S. and M.Ke.; funding acquisition, R.S. and M.Ke. All authors have read and agreed to the published version of the manuscript.

Appendix A. The mesh independence study

The mesh independence study was conducted for all three simulation cases: For Case I (the concentric cylinder), we investigated the standard numerical approach. For Case II (one impeller), we evaluated the mesh option where we used the circular mesh with the large diameter around the impeller and the large passive area at the background mesh. In these cases, both the single mesh and overset mesh simulations were studied while for Case III (two impellers), only the overset mesh simulation was evaluated.

The representative cell sizes were calculated as follows:

$$h = \sqrt{\frac{1}{N}\sum A_i}, \tag{11}$$

where N and A_i were the number of cells and the cell area, respectively. The representative cell sizes are summarized in Tab. 4, and the figures of the applied mesh densities are presented in Figs. 18-22.

For the mesh independence study, N_p and the velocity fields were investigated. The total N_p values are summarized in Tab. 5. The velocity profiles for Case I and II are presented in Figs. 23 and 24, respectively. For Case III, the velocity fields is presented in Fig. 25 and the velocity components along vertical line in Fig. 26 and horizontal in Fig. 27. These results indicated that refining the mesh beyond the medium mesh density did not affect the results significantly and thus, the medium mesh density applied in the simulations was sufficient for the present work.

Table 4. The representative cell sizes of the applied mesh densities for the different simulation cases where D is the diameter of rotating cylinder or the impeller.

		coarse	medium	refined medium	fine
Case I	single mesh	0.070D	0.048D	-	0.035D
	overset mesh	0.061D	0.043D	-	0.031D
Case II	single mesh	0.056D	0.039D	-	0.028D
	overset mesh	0.049D	0.034D	-	0.025D
Case III	single mesh	-	-	-	-
	overset mesh	-	0.018D	0.014D	0.012D

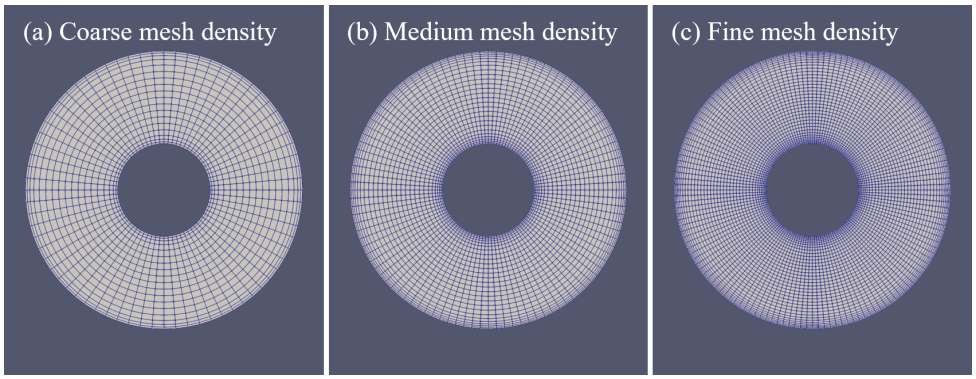

Figure 18. The mesh densities for Case I when using single mesh method.

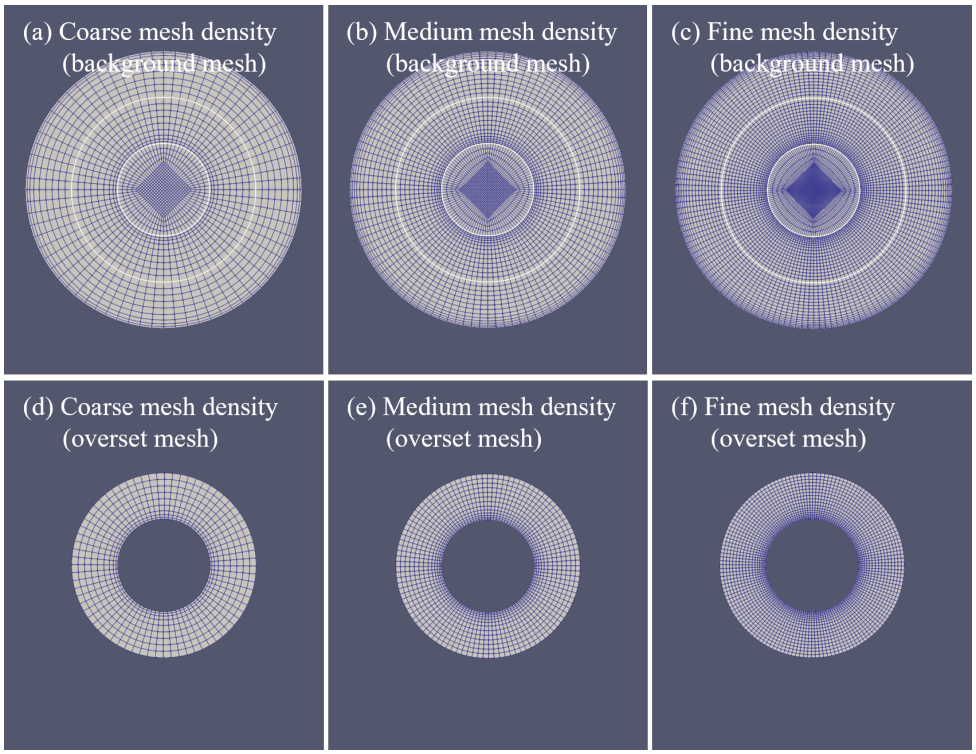

Figure 19. The mesh densities for Case I when using overset mesh method.

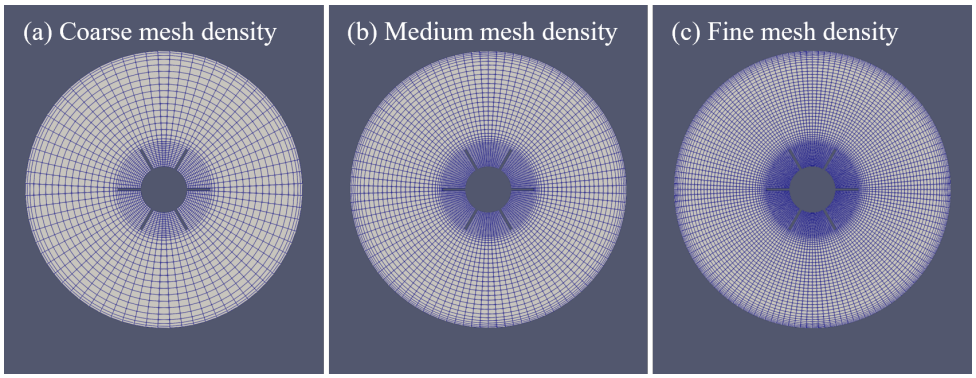

Figure 20. The mesh densities for Case II when using single mesh method.

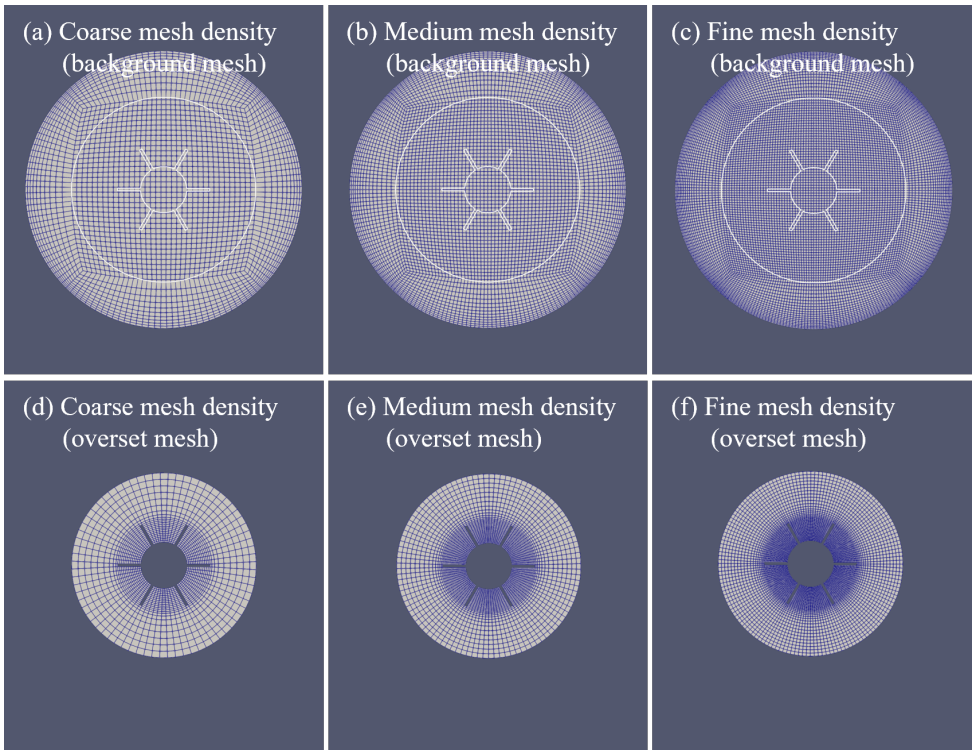

Figure 21. The mesh densities for Case II when using overset mesh method.

Table 5. The mean N_p for different simulation cases at the steady state conditions. The applied abbreviations are as follows: left – the left impeller, and right – the right impeller.

		coarse	medium	refined medium	fine
Case I	single mesh	43.9	43.8	-	43.9
	overset mesh	43.7	43.8	-	43.8
Case II	single mesh	12.0	12.1	-	12.2
	overset mesh	12.1	12.3	-	12.2
Case III	single mesh	-	-	-	-
	overset mesh	-	left: 41.4 right: 41.8	left: 40.4 right: 41.0	left: 42.1 right: 42.4

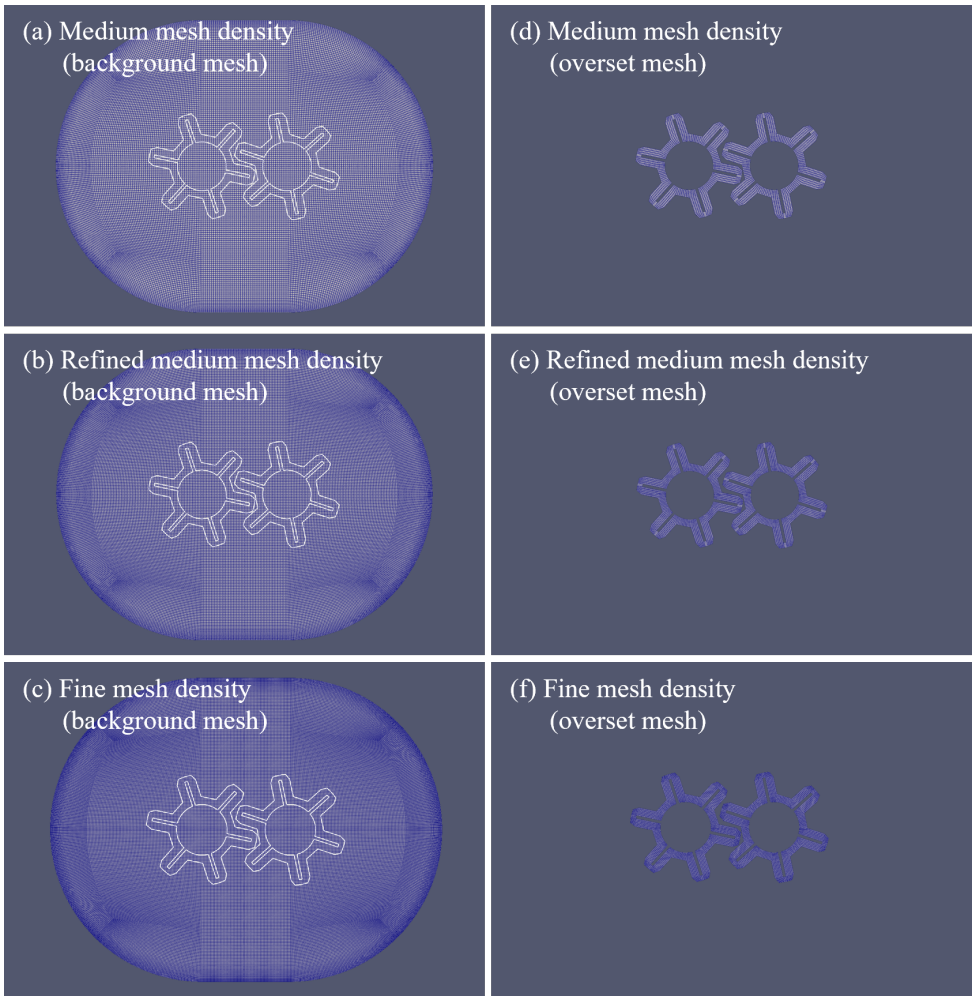

Figure 22. The mesh densities for Case III when using overset mesh method.

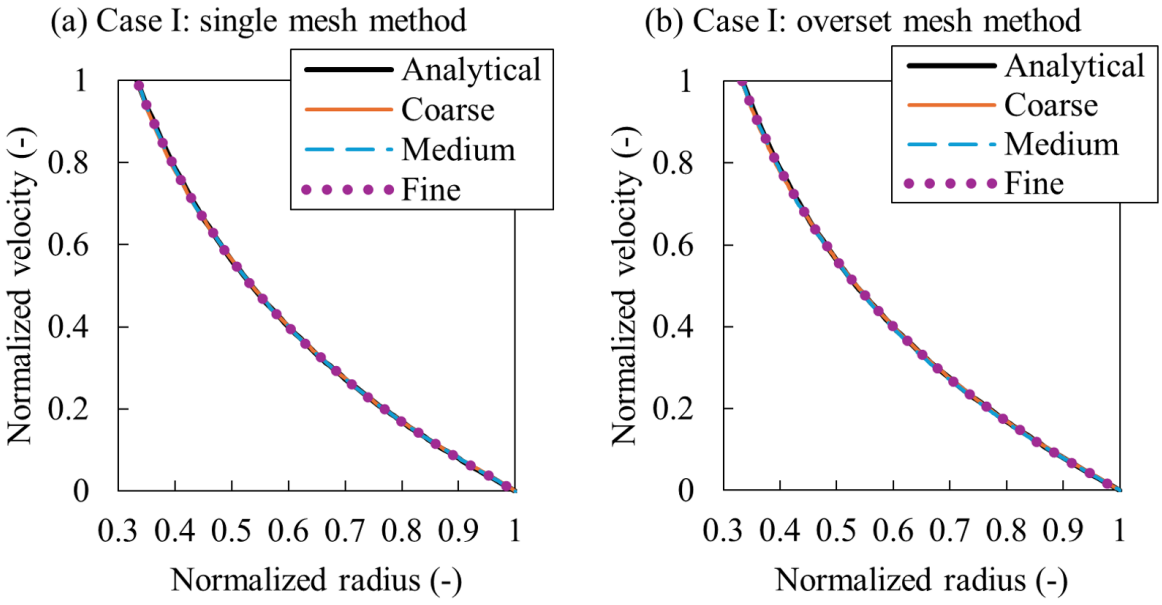

Figure 23. Case I: The velocity profiles obtained from three mesh densities along the radius utilizing (a) the single mesh method, and (b) the overset mesh method.

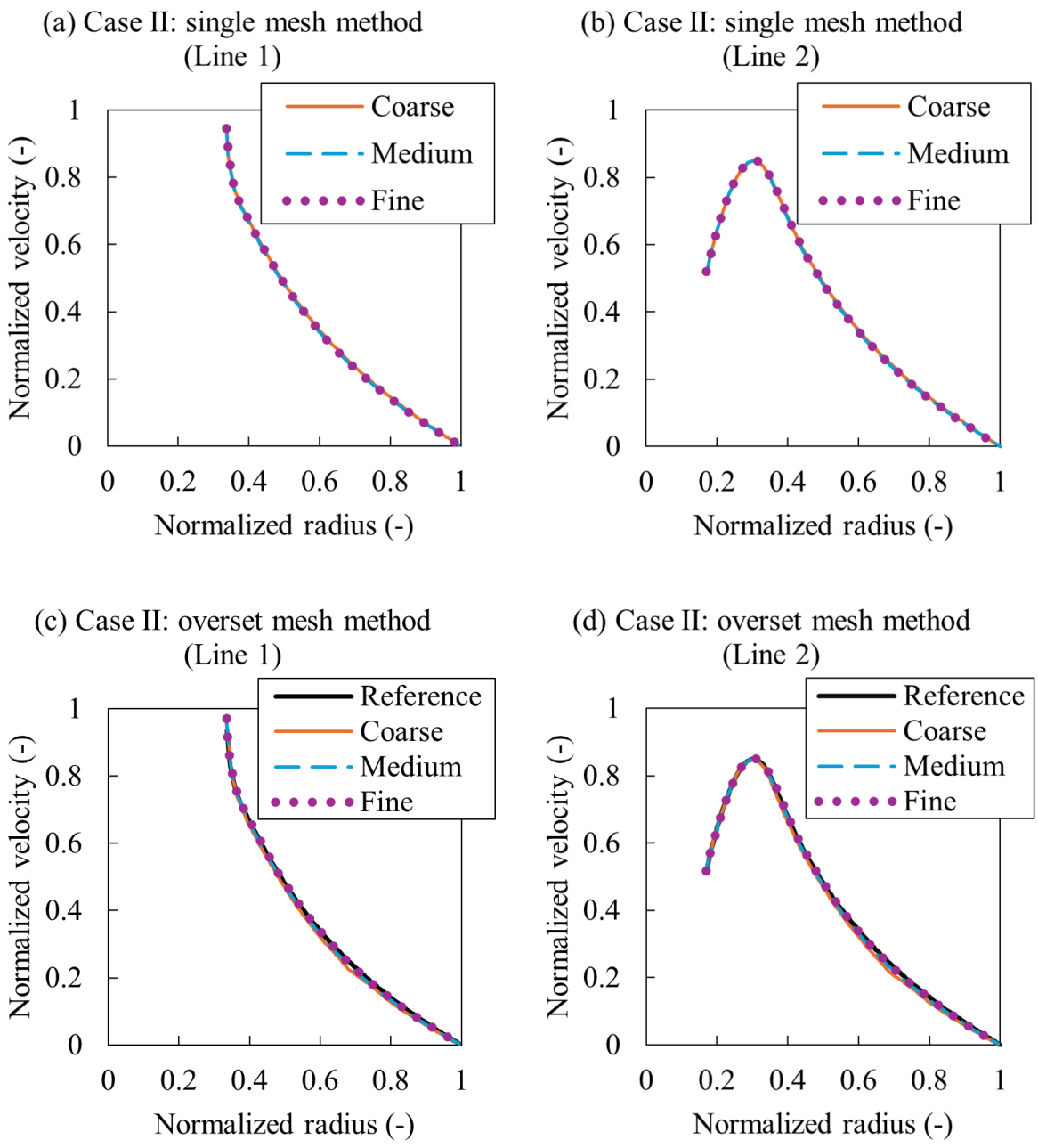

Figure 24. Case II: The velocity profiles obtained from three mesh densities along one blade (Line 1) and between two blades (Line 2) the utilizing the single mesh method in (a)-(b), and the overset mesh method in (c)-(d).

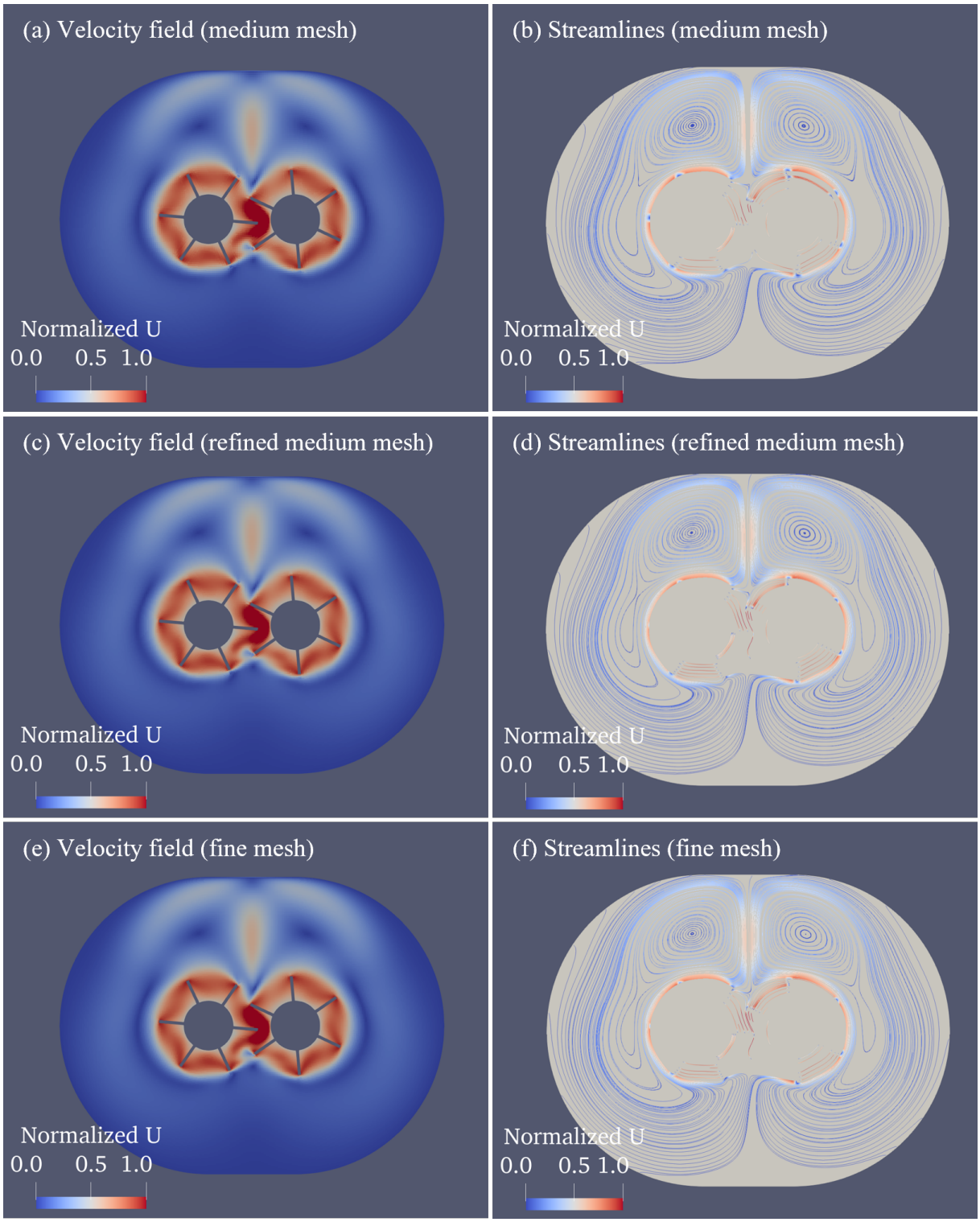

Figure 25. Case III: The velocity fields and streamlines obtained from three mesh densities utilizing the overset mesh method.

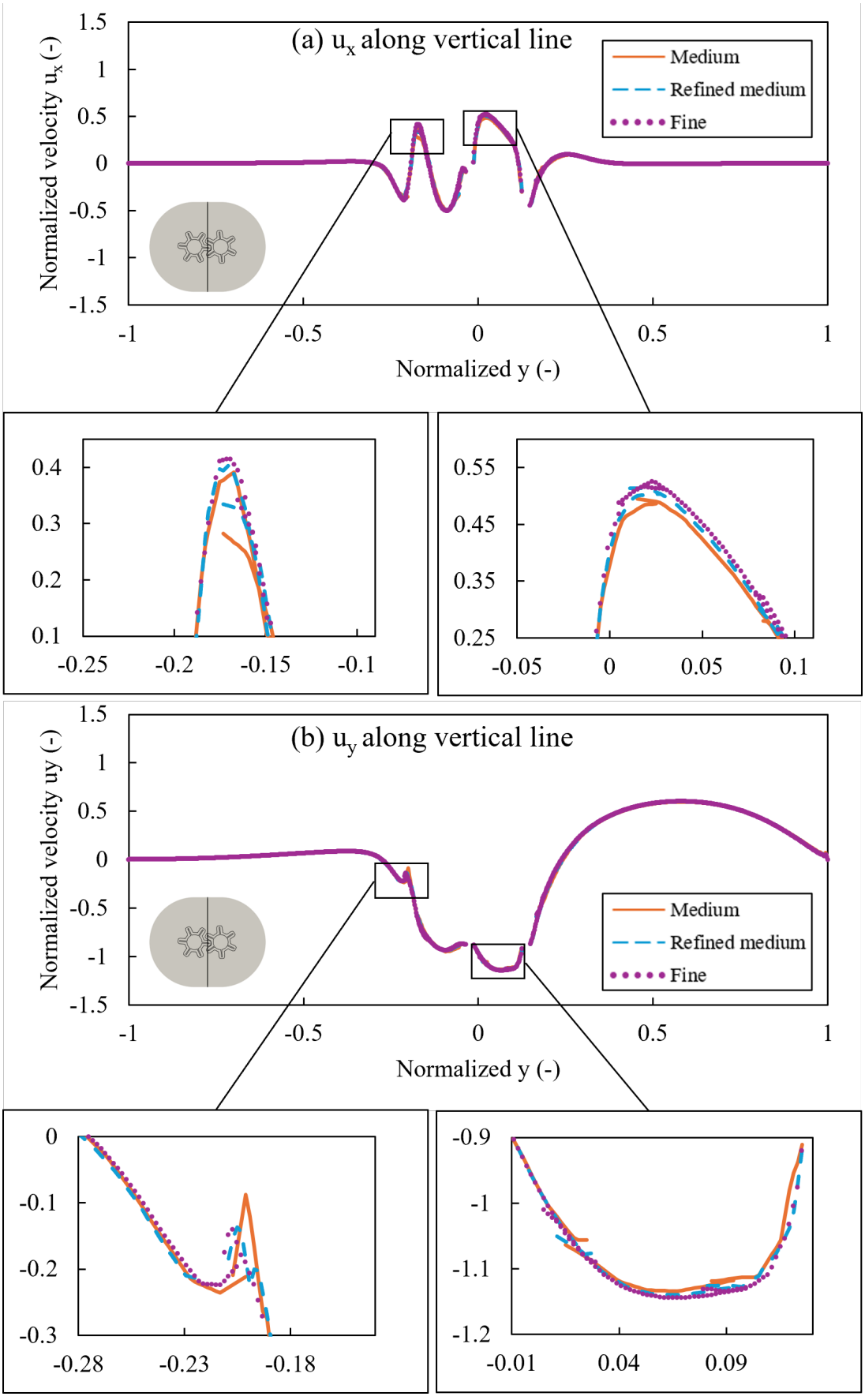

Figure 26. Case III: The velocity along vertical line (a) u_x and (b) u_y.

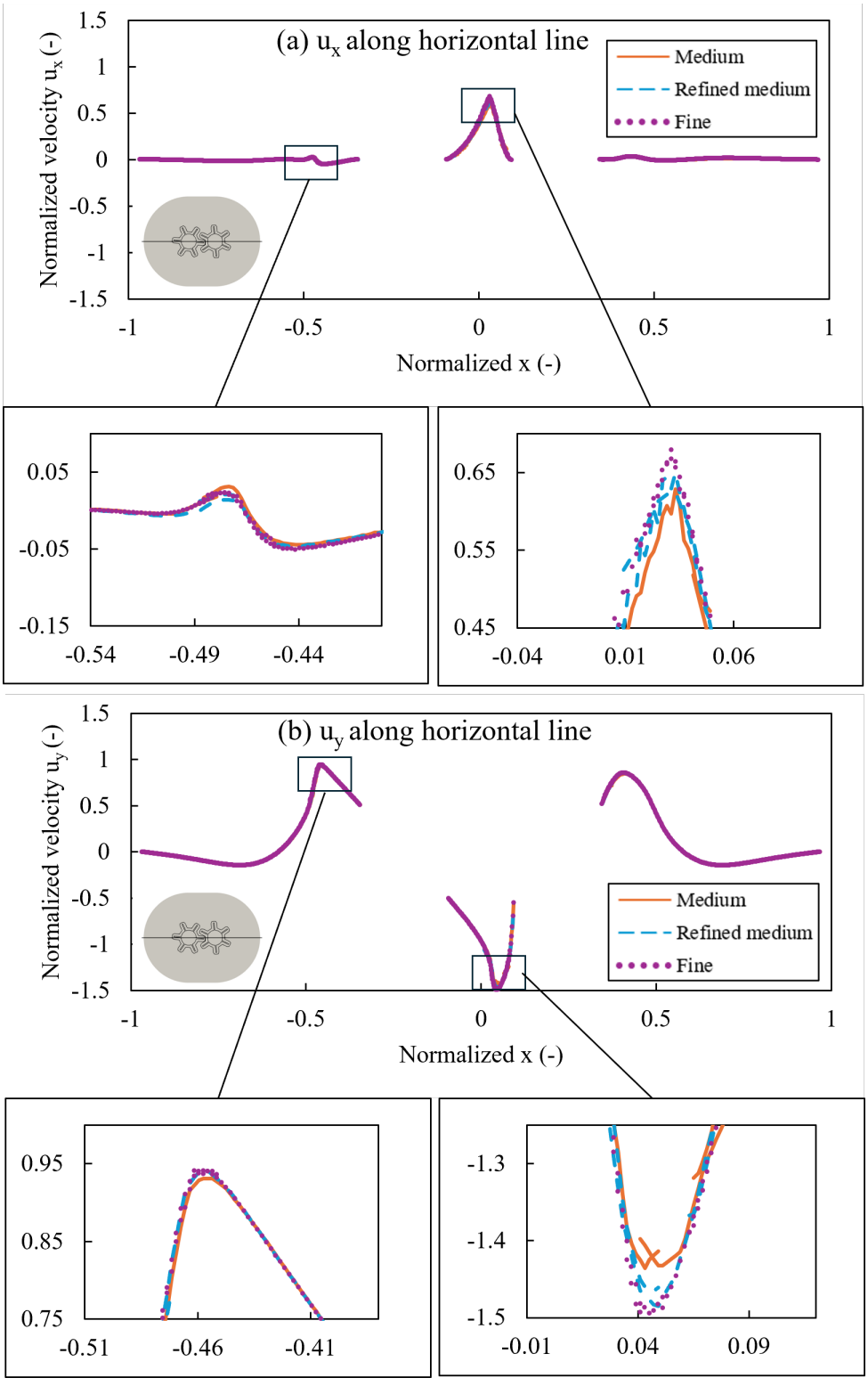

Figure 27. Case III: The velocity along horizontal line (a) u_x and (b) u_y.

References

[1] T. Ishikawa, S.-I. Kihara, and K. Funatsu, "3-D numerical simulations of nonisothermal flow in co-rotating twin screw extruders," *Polymer Engineering & Science*, vol. 40, no. 2, pp. 357–364, 2000.

[2] M. Yoshinaga, S. Katsuki, M. Miyazaki, L. Liu, S.-I. Kihara, and K. Funatsu, "Mixing mechanism of three-tip kneading block in twin screw extruders," *Polymer Engineering and Science*, vol. 40, no. 1, pp. 168–178, 2000.

[3] T. Avalosse, "Numerical simulation of distributive mixing in 3-D flows," *Macromolecular Symposia*, vol. 112, no. 1, pp. 91–98, 1996.

[4] W. Cheng, Y. Ye, S. Jiang, J. Wang, X. Gu, and L. Feng, "Mixing intensification in a horizontal self-cleaning twin-shaft kneader with a highly viscous Newtonian fluid," *Chemical Engineering Science*, vol. 201, pp. 437–447, 2019.

[5] Y. Shuai, S. An, X. Hong, Z. Huang, Z. Liao, J. Wang, and Y. Yang, "Numerical Simulation of Hydrodynamics and Mixing Characteristics of High-Viscosity Non-Newtonian Fluid in Twin-Shaft Kneaders," *Industrial & Engineering Chemistry Research*, vol. 63, no. 13, pp. 5931–5941, 2024.

[6] B. Alsteens, V. Legat, and T. Avalosse, "Parametric study of the mixing efficiency in a kneading block section of a twin-screw extruder," *International polymer processing*, vol. 19, no. 3, pp. 207–217, 2004.

[7] S. Yamada, K. Fukutani, K. Yamaguchi, H. Funahashi, K. Ebata, H. Uematsu, and S. Tanoue, "Dispersive Mixing Performance Evaluation of Special Rotor Segments in an Intermeshing Co-Rotating Twin-Screw Extruder by Using Weighted Probability Distributions," *International Polymer Processing*, vol. 30, no. 4, pp. 451–459, 2015.

[8] M. A. Emin, P. Wittek, and Y. Schwegler, "Numerical analysis of thermal and mechanical stress profile during the extrusion processing of plasticized starch by non-isothermal flow simulation," *Journal of Food Engineering*, vol. 294, 2021.

[9] F. Bertrand, P. A. Tanguy, and F. Thibault, "A three-dimensional fictitious domain method for incompressible fluid flow problems," *International Journal for Numerical Methods in Fluids*, vol. 25, no. 6, pp. 719–736, 1997.

[10] R. Giguère, F. Bertrand, and P. A. Tanguy, "A three-dimensional mesh refinement strategy for the simulation of fluid flow with a fictitious domain method," *Computers and Chemical Engineering*, vol. 30, no. 3, pp. 453–466, 2006.

[11] B. Alsteens, "Mathematical modelling and simulation of dispersive mixing," Ph.D. Dissertation, Université catholique de Louvain, Louvain-La-Neuve, Belgium, May 2005. [Online]. Available: http://hdl.handle.net/2078.1/5199

[12] A. Sarhangi Fard, M. A. Hulsen, H. E. H. Meijer, N. M. H. Famili, and P. D. Anderson, "Tools to Simulate Distributive Mixing in Twin-Screw Extruders," *Macromolecular Theory and Simulations*, vol. 21, no. 4, pp. 217–240, 2012.

[13] J. Benek, P. Buning, and J. Steger, "A 3-d chimera grid embedding technique," in *7th Computational Physics Conference*, 1985. [Online]. Available: https://arc.aiaa.org/doi/pdf/10.2514/6.1985-1523

[14] A. Singh Tomar, H. K G, and K. A. Prakash, "Numerical estimation of thermal load in a three blade vertically agitated mixer," *E3S Web of Conferences*, vol. 128, p. 08004, 2019.

[15] Z. Gao, J. Li, X. Shao, and L. Zeng, "Numerical Simulation and Aerodynamic Investigation of the Intermeshing Rotor in Hover," *Journal of Physics: Conference Series*, vol. 2252, no. 1, p. 012056, 2022.

[16] S. Völkner, J. Brunswig, and T. Rung, "Analysis of non-conservative interpolation techniques in overset grid finite-volume methods," *Computers & Fluids*, vol. 148, pp. 39–55, 2017.

[17] D. D. J. Chandar, "On overset interpolation strategies and conservation on unstructured grids in OpenFOAM," *Computer Physics Communications*, vol. 239, pp. 72–83, 2019.

[18] D. D. J. Chandar and J. Sitaraman, "A flux correction approach for the pressure equation in incompressible flows on overset meshes in OpenFOAM," *Computer Physics Communications*, vol. 273, p. 108279, 2022.

[19] G. Zhang, J. Wang, Y. Feng, H. Jin, Q. Ge, X. Xu, and J. Li, "Experimental and numerical investigation on the hydrodynamic performance of an amphibious vehicle under the interaction of traveling mechanism mudguard and waterjet propulsor duct," *Ocean engineering*, vol. 340, pp. 122 426–, 2025.

[20] S. Đurasević, I. Gatin, T. Uroić, and H. Jasak, "Numerical analysis of self-propulsion flow characteristics in model scale," *Ocean Engineering*, vol. 259, p. 111885, 2022.

[21] M. Lakatoš, S. Mancini, R. Niazmand Bilandi, and K. Tabri, "Verification and validation of hard-chine hull performance in calm water: Effects of numerical setups and hull configurations," *Ocean engineering*, vol. 329, pp. 121 056–, 2025.

[22] E. W. Quon and M. J. Smith, "Advanced data transfer strategies for overset computational methods," *Computers & fluids*, vol. 117, pp. 88–102, 2015.

[23] E. Rinaldi, P. Colonna, and R. Pecnik, "Flux-conserving treatment of non-conformal interfaces for finite-volume discretization of conservation laws," *Computers & fluids*, vol. 120, pp. 126–139, 2015.

[24] A. Sharma, S. Ananthan, J. Sitaraman, S. Thomas, and M. A. Sprague, "Overset meshes for incompressible flows: On preserving accuracy of underlying discretizations," *Journal of computational physics*, vol. 428, pp. 109 987–, 2021.

[25] A. Eitzlmayr and J. Khinast, "Co-rotating twin-screw extruders: Detailed analysis of conveying elements based on smoothed particle hydrodynamics. Part 1: Hydrodynamics," *Chemical Engineering Science*, vol. 134, pp. 861–879, 2015.

[26] A. Eitzlmayr, J. M. Maticánd, and J. Khinast, "Analysis of Flow and Mixing in Screw Elements of Corotating Twin-Screw Extruders via SPH," *American Institute of Chemical Engineers*, vol. 63, no. 6, pp. 2451–2463, 2017.

[27] W. Zhang, Q. Jiang, G. Bois, H. Li, X. Liu, S. Yuan, and Y. Heng, "Experimental and Numerical Analysis on Flow Characteristics in a Double Helix Screw Pump," *Energies*, vol. 12, no. 18, 2019.

[28] M. Yamakawa, N. Mitsunari, and S. Asao, "Numerical Simulation of Rotation of Intermeshing Rotors using Added and Eliminated Mesh Method," *Procedia Computer Science*, vol. 108, pp. 1883–1892, 2017.

[29] E. Askari, G. St-Pierre Lemieux, and P. Proulx, "Application of extended quadrature method of moments for simulation of bubbly flow and mass transfer in gas-liquid stirred tanks," *The Canadian Journal of Chemical Engineering*, vol. 97, no. 9, pp. 2548–2564, 2019.

[30] X. Hu, A. D. Ilgun, A. Passalacqua, R. O. Fox, F. Bertola, M. Milosevic, and F. Visscher, "Cfd simulations of stirred-tank reactors for gas-liquid and gas-liquid-solid systems using OpenFOAM®," *International Journal of Chemical Reactor Engineering*, vol. 19, no. 2, pp. 193–207, 2021.

[31] G. S. Berestinas and J. R. Nunhez, "Experimental and computational investigation of coaxial contra-rotating impellers design in baffled-free stirred reactors," *The Canadian Journal of Chemical Engineering*, vol. 102, no. 8, pp. 2663–2681, 2024.

[32] A. Reid, R. Rossi, C. Cottini, and A. Benassi, "Cfd simulation of a rushton turbine stirred-tank using open-source software with critical evaluation of mrf-based rotation modeling," *Meccanica*, vol. 60, no. 6, pp. 1613–1637, 2024.

[33] R. Bannari, A. Bannari, B. Selma, and P. Proulx, "Mass transfer and shear in an airlift bioreactor: Using a mathematical model to improve reactor design and performance," *Chemical Engineering Science*, vol. 66, no. 10, pp. 2057–2067, 2011.

[34] F. Ramonet, M. Kovacevic, B. Haddadi, C. Jordan, and M. Harasek, "Bioreactor Mixing: a Comparison of Computational Fluid Dynamics and Experimental Approaches in the Pursuit of Sustainable Bioprocessing for the Bioeconomy," *Chemical Engineering Transactions*, vol. 105, pp. 265–270, 2023.

[35] S. Huang, Y. Hu, Y. Wei, and Y. Mo, "Analysis of Cavitation Flow Performance in Centrifugal Pump Using OpenFOAM," *Journal of Physics: Conference Series*, vol. 2610, no. 1, p. 012023, 2023.

[36] W. Zhao, M. Wang, B. Liang, L. Zhao, and Q. Liu, "Study of transient pressure and fluctuation characteristics in a centrifugal pump using the delayed detached-eddy simulation method," *Intelligent Marine Technology and Systems*, vol. 2, no. 1, p. 31, 2024.

[37] G. Chen, C. Gu, H. Hajaiej, P. J. Morris, E. G. Paterson, and A. Sergeev, "OpenFOAM computation of interacting wind turbine flows and control (I): free rotating case," *International Journal of Hydromechatronics*, vol. 4, no. 1, pp. 1–26, 2021.

[38] O. D. Lopez Mejia, O. E. Mejia, K. M. Escorcia, F. Suarez, and S. Laín, "Comparison of Sliding and Overset Mesh Techniques in the Simulation of a Vertical Axis Turbine for Hydrokinetic Applications," *Processes*, vol. 9, no. 11, p. 1933, 2021.

[39] S. Salehi, H. Nilsson, E. Lillberg, and N. Edh, "Numerical simulation of hydraulic turbine during transient operation using openfoam," *IOP Conference Series. Earth and Environmental Science*, vol. 774, no. 1, p. 12060, 2021.

[40] H. C. Önel, A. A. Adam, and N. S. Uzol, "Comparative Aerodynamic Analysis and Parallel Performance of 2D CFD Simulations of a VAWT Using Sliding Mesh Interface Method," *Concurrency and Computation: Practice and Experience*, vol. 37, no. 3, p. e8353, 2025.

[41] N. Casari, E. Fadiga, M. Pinelli, A. Suman, and D. Ziviani, "Cfd simulations of single- and twin-screw machines with openfoam," *Designs*, vol. 4, no. 1, p. 2, 2020.

[42] H. Jasak, "Dynamic mesh handling in openfoam," in *47th AIAA Aerospace Sciences Meeting including the New Horizons Forum and Aerospace Exposition*. Orlando, Florida, USA: American Institute of Aeronautics and Astronautics, 2009.

[43] J. H. Ferziger and M. Peric, *Computational Methods for Fluid Dynamics*. Berlin, Heidelberg, Germany: Springer Berlin / Heidelberg, 1996.

[44] C. Greenshields and H. Weller, *Notes on Computational Fluid Dynamics: General Principles*. Reading, UK: CFD Direct Ltd, 2022.

[45] F. M. White, *Viscous fluid flow*, 3rd ed. Boston, MA, USA: McGraw-Hill, 2006.

[46] H. Patil, A. K. Patel, H. J. Pant, and A. Venu Vinod, "CFD simulation model for mixing tank using multiple reference frame (MRF) impeller rotation," *ISH Journal of Hydraulic Engineering*, vol. 27, no. 2, pp. 200–209, 2021.

[47] H. Jasak, H. Weller, and A. Gosman, "High resolution NVD differencing scheme for arbitrarily unstructured meshes," *International Journal for Numerical Methods in Fluids*, vol. 31, no. 2, pp. 431–449, 1999.

[48] CSC – IT Center for Science, Finland, "Puhti – csc supercomputer system," https://docs.csc.fi/computing/systems-puhti/, 2025, accessed: 8 Nov 2025.